This is to certify that the
thesis entitled

DESIGN AND ANALYSIS OF A WIDEBAND PATCH
ANTENNA FOR USE WITH A MINIATURE RADAR SYSTEM

presented by

NATHAN THOMAS KORNBAU

has been accepted towards fulfillment
of the requirements for the

Master of Science degree in Electrical Engineering

Major Professor's Signature

02 May 2008

Date

DESIGN AND ANALYSIS OF A WIDEBAND PATCH ANTENNA FOR USE WITH A MINIATURE RADAR SYSTEM

By

Nathan Thomas Kornbau

A THESIS

Submitted to
Michigan State University
in partial fulfillment of the requirements
for the degree of

MASTER OF SCIENCE

Department of Electrical Engineering

2008

ABSTRACT

DESIGN AND ANALYSIS OF A WIDEBAND PATCH ANTENNA FOR USE WITH A MINIATURE RADAR SYSTEM

By

Nathan Thomas Kornbau

A radar system that operates in the high X-band and low-Ku band is being developed for use on a miniature unmanned air vehicle(Mini-UAV). For the system to meet electrical and weight requirements a custom high bandwidth (15% or more), linearly polarized, low profile antenna is required. Resonant microstrip patch antennas are generally linearly polarized and have a low profile construction. However, like all resonant antennas, microstrip patch antennas have low bandwidth, usually around 3% to 5%. Due to the other favorable characteristics of patch antennas, large amounts of research have been performed to increase the their bandwidth. This thesis examines the use of an array of four identical passive patches symmetrically positioned above a fifth driven patch antenna buried between two dielectric substrates. The four patches are excited by coupling with the driven patch. The coupling between the patches also results in an increase in bandwidth. Simulations using a commercial finite element method solver were performed to find an antenna design to potentially meet the Mini-UAV bandwidth requirements. The simulated design was then fabricated and experimentally tested to verify the simulation results. The simulation and experimental procedure and results will be presented in this thesis.

at

su

I

K

n.

ACKNOWLEDGMENTS

I would like to thank Dr. Leo Kempel, for the opportunity to work and study at this institution. I would also like thank Dr. Ed Rothwell and Dr. Shanker Balasubramaniam for sharing their vast knowledge with me over the past couple of years. I am grateful for the assistance and support provided by Dr. Jeff Berrie and Dave Kuhl before and during the work performed for this research. Finally, thank you to my parents, Tom and Millie, for their everlasting love and encouragement.

TABLE OF CONTENTS

LIST OF TABLES

LIST OF FIGURES

F

F
F
F
F
F

Fi

Fi

Fi

Fi

Fi

Fi

Fi

Fi

Fi

Fi

F

F
F
F
F
F

1.

Th

B

Di

b

C

op

th

of

ti

ti

is

of

W

n

c

2

CHAPTER 1

INTRODUCTION

1.1 Motivation

This research project was a collaborative effort between Michigan State University, BerrieHill Research Corporation, Air Force Research Laboratories (AFRL) Sensors Directorate to design an antenna for use with a miniature radar system that will be mounted on an Air Force(USAF) Miniature Unmanned Air Vehicle(Mini-UAV). Currently the Mini-UAV has an optical sensor that is capable of sending video to the operator, however adding a small radar system will allow a larger field of view and the ability of the Mini-UAV to detect objects through rain, fog, dust, and smoke all of which hinder the usefulness of the optical sensor [4].

The miniature radar is currently in development at BerrieHill Research Corporation, the radar will have three modes of operation, Ground Moving Target Indication(GMTI), High range resolution(HRR), and Synthetic Aperture Radar (SAR). It is being designed to operate in the high X and low Ku bands with a center frequency of 12.5 GHz and a bandwidth of 1.9 GHz (15% bandwidth) with a Voltage Standing Wave Ratio(VSWR) less than 2.

In addition to the radio frequency(RF) requirements there are also physical and monetary restrictions. The Mini-UAV has a limited load carrying capacity so the complete radar system must weigh less than $4kg$ and a total volume less than $20cm$ x $20cm$ x $10cm$. It is also desired to keep the cost of the radar system low so in the case that a Mini-UAV is lost or damaged there is a minimal monetary loss. The goal of this thesis is to design, fabricate, and test an antenna that meets the RF and physical requirements while keeping manufacturing and material costs to a minimum.

1.2 Design Specifications

As was presented in the previous section the antenna design must meet several criteria. The RF or electrical requirements will be the most important requirements to meet. In addition to the center frequency being at 12.5 GHz and a 15% bandwidth with a VSWR less than 2, the antenna also needs to be linearly polarized. This will allow the most energy possible to be re-absorbed by the antenna as the Mini-UAV moves by keeping the antenna allgined withthe transmitted signal on its return trip. Also, the pattern of the antenna should have only a single lobe.

The physical, manufacturing simplicity and monetary criteria are dependent on one another. For example, a certain material will strongly influence the cost of the antenna, the manufacturing ease, and the weight of the antenna. To meet all of these requirements a resonant microstrip antenna design was selected. Microstrip antennas are very simple mechanically, so can be manufactured using standard circuit board processing techniques. Also, they are lightweight consisting only of sheets of dielectric material and thin layers of copper. The dielectric material is relatively inexpensive and easily obtainable from various manufacturers. Using a microstrip antenna design also offers another advantage, the radar system requires a way of running signals from the RF source to the antenna. The sources will be located behind the antenna so the feeds will preferably be able to bend a certain degree. If a flexible dielectric material is

ma

ele

pa

pa

th

of

b

an

an

th

1.

T

m

b

T

o

b

is this can easily be done by using microstrip transmission lines on the same piece of material as the antenna, minimizing the use of connectors and cables.

The resonant microstrip antenna, or patch antenna, also meets several of the electrical criteria as well. They can radiate lineraly polarized and the pattern of patch antennas consists of a single lobe. However, a considerable draw back is that patch antennas generally have a very limited bandwidth, around 2% to 5%, much less than the bandwidth required by the radar system [3].

Due to the many positive features of patch antennas, low profile, size, and ease of fabrication, much work has been done observing the methods of increasing their bandwidth. Two methods are available to increase bandwidth, structural techniques and a circuit theory approach [14]. In this thesis ideas from both of these methods are used to design a resonant patch antenna that meets bandwidth requirements of the miniature radar system.

1.3 Overview

The second chapter will review the theory behind resonant patch antennas and basic microstrip transmission lines. The third chapter will discuss methods of increasing bandwidth of patch antennas and the general design used for this thesis.

Chapter 4 will introduce the simulation methods used for the antenna design. The final part of Chapter 4 will show simulation results and identify trends that were observed while the design was being tuned.

The process that was used to fabricate the antenna designs from Chapter 4 will be shown in Chapter 5. This chapter will also describe the tests that were performed on the fabricated antennas and present the results from the tests.

The final chapter will contain conclusions and recommendations for future work based the research performed for this thesis.

CHAPTER 2

PATCH ANTENNA THEORY

Since this thesis examines the use of a variation of a basic patch antenna using a microstrip transmission line as a feed, this chapter will first briefly review some background theory behind basic microstrip transmission lines. Following this section the theory behind a single rectangular microstrip patch antenna will be presented.

2.1 Microstrip Transmission Line Theory

Microstrip transmission lines will be the easiest way to feed a patch antenna, they can be fabricated in the same way and at the same time as the patch antenna. The basic geometry of of a microstrip transmission line is shown below in Figure 2.1. The most basic way to analyze a microstrip transmission line is to assume the substrate has a dielectric constant of one and use image theory with the ground plane to setup a simple transverse electromagnetic(TEM) transmission line [9].

However, cases where the substrate's dielectric constant is not one, especially when there is air above the conducting material, are significantly more complicated. In these cases a true TEM wave cannot exist due to the differing phase velocities in each of the materials. If the substrate is electrically very thin, $d << \lambda$, a quasi-TEM wave exists where most of the field energy is located in the substrate with the highest concentration below the conducting material as shown in Figure 2.2. In the quasi-TEM case analysis can be used to provide accurate approximations of transmission line impedance [9].

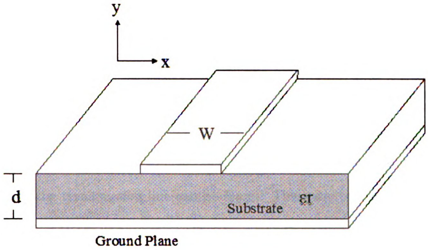

Figure 2.1. The geometry of a microstrip transmission line.

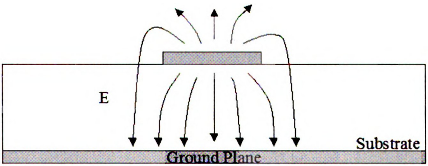

Figure 2.2. The field sturcture of microstrip transmission line.

The width of the conducting line, height of the substrate and the dielectric constant of the substrate all contribute to the impedance of the transmission line. First, an effective dielectric constant, ϵ_e, must be found since both air and the substrate must be considered to find the line impedance(2.1).

$$\epsilon_e = \frac{\epsilon_r + 1}{2} + \frac{\epsilon_r - 1}{2}\frac{1}{\sqrt{1 + 12d/W}} \tag{2.1}$$

Using the effective dielectric in the following equations the characteristic impedance of the transmission line can be found. There are two equations for cases when the ratio of W/d is larger or smaller than one. For a ratio larger than one (2.2) is used.

$$Z_o = \frac{60}{\sqrt{\epsilon_e}} \ln\left(\frac{8d}{W} + \frac{W}{4d}\right) \tag{2.2}$$

For a ratio smaller than one (2.3) is used.

$$Z_o = \frac{120\pi}{\sqrt{\epsilon_e}[W/d + 1.393 + 0.667\ln(W/d + 1.444)]} \tag{2.3}$$

A more detailed explanation of how there equations were obtained is presented in [9]. These equations will be used later in the design stage of the antenna to find the width needed to create a microstrip transmission line with an impedance of 50Ω.

2.2 Patch Antenna Background Theory

A typical patch antenna consists of a dielectric material (substrate) sandwiched between a conducting patch and a conducting ground plane. Any shape of the conducting patch can be used, however, for this thesis a rectangular patch, similar to the patch shown in Figure 2.3, is examined. The best way to analyze a patch antenna is to treat the volume underneath the patch as a lossy resonant cavity where instead of all the energy being dissipated in the dielectric material it is radiated from the sides of the cavity. A patch antenna shares another properties with a resonant cavity, typically both have a very narrow bandwidth of only a few percent. This narrow bandwidth is a feature shared by all resonant type antennas. Also, like a cavity, the dimensions of the patch determine the frequency at which the resonance occurs, the frequency that radiates [13].

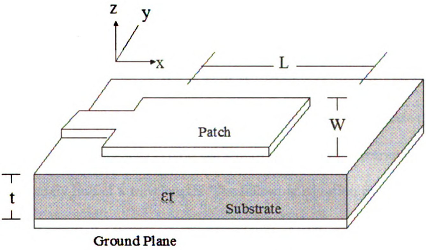

Figure 2.3. The geometry of a patch antenna fed by a microstrip transmission line.

As shown in Figure 2.3 this thesis will look at the case of a patch where L is approximately half of a wavelength and is fed by a microstrip transmission line. The

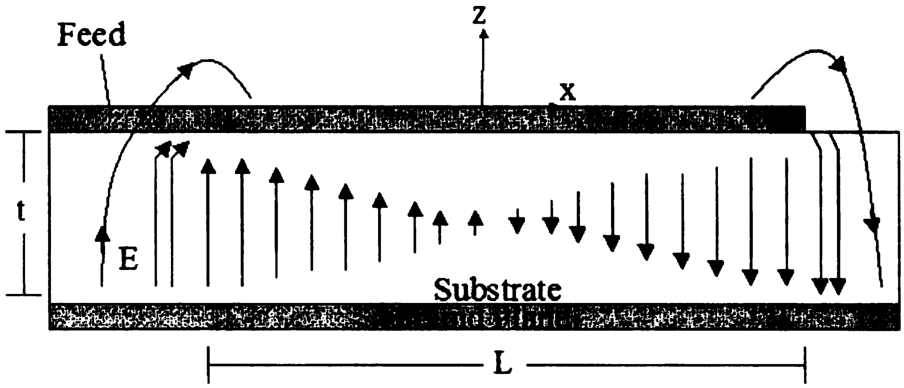

Figure 2.4. The side view of a patch antenna showing the electric field structure underneath the patch.

half wavelength patch will allow the patch to resonant at the desired frequency and have a real impedance. The feed will transport energy in to the volume underneath the patch, here a standing wave will form as shown in Figure 2.4, similar to a parallel plate capacitor. However, since the ends of the patch are open it can be seen that some fringing occurs at the edges of the patch. These fringing fields cause the patch to radiate. The fringing fields also extend the length of the patch electrically, this is why L is approximately half of a wavelength. The following equation provides an estimate of the physical value of L based on the wavelength, λ, and dielectric constant, ϵ_r, of the substrate [13].

$$L = 0.49\frac{\lambda}{\sqrt{\epsilon_r}} \tag{2.4}$$

In the xz-plane the fields at the edges of the patch are identical in magnitude however they have opposite z-components, thus cancel each other out.When viewed

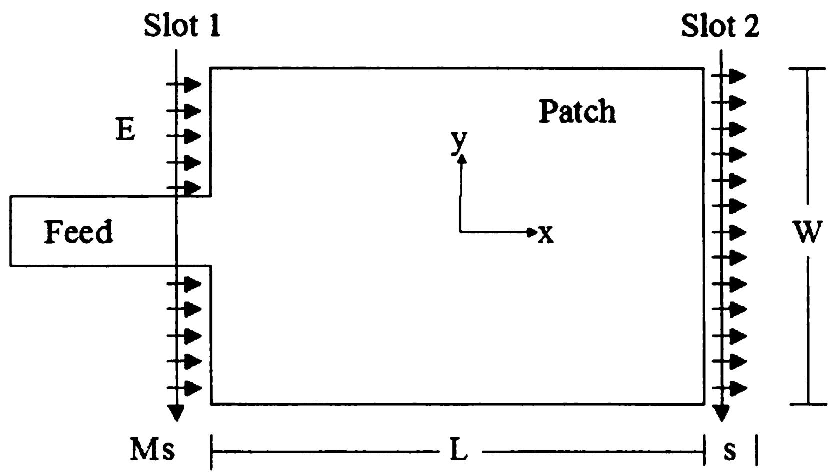

Figure 2.5. The top view of a patch antenna showing the "slots" created by electric field fringing.

from the top, Figure 2.5, it can be seen that in the xy-plane the electric fields have the same phase, this causes radiation and the broadside pattern of patch antennas. In cases where the substrate thickness is much thinner than a wavelength the width of the fringing fields, s, can be approximated to be the same as the substrate thickness. The areas of the fringing fields can best be analyzed by being treated as slot apertures of length s and and width W. To show the field pattern of a patch antenna the pattern from one of the two slots must be calculated and then array theory must be applied to account for the second identical slot [7].

In order to solve the slot field patterns the electric fields in the slots, E_a, must be converted to magnetic surface currents, M_s. This relationship is shown below in (2.5) [5].

$$\vec{Ms} = \vec{Ea} \times \hat{n} \tag{2.5}$$

Using the magnetic current the electric vector potential, F, can be found, (2.6).

$$\vec{F} = \epsilon\frac{exp(-j\beta r)}{4\pi r}\int\int_S \vec{M}s(r')exp(j\beta\hat{r}\cdot r')dS' \tag{2.6}$$

Substitute (2.5) into (2.6) results in the electric vector potential in terms of the electric field in the area of the slot, S_a.

$$\vec{F} = \epsilon\frac{exp(-j\beta r)}{4\pi r}\hat{n}\times\int\int_{Sa} \vec{E_a}exp(j\beta\hat{r}\cdot r')dS' \tag{2.7}$$

From Figure 2.5 it can be observed that E_a only has x-components, so E_a can be written as $E_s = E_o\hat{x}$. The magnitude of the electric field is represented by E_o. Also, in this situation $\hat{n}$ in is the z-direction, $\hat{z}$. Making these substitutions in (2.7) results in (2.8) [7].

$$\vec{F} = \epsilon\frac{exp(-j\beta r)}{4\pi r}\hat{z}\times\int\int_{Sa} E_o\hat{x}exp(j\beta\hat{r}\cdot r')dS' \tag{2.8}$$

Taking the cross product of (2.8).

$$\vec{F} = \hat{y}E_o\epsilon\frac{exp(-j\beta r)}{4\pi r}\int\int_{Sa} exp(j\beta\hat{r}\cdot r')dS' \tag{2.9}$$

Based the the shape the of the slot the source coordinates should be chosen to be in the cartesian system, $r' = x'\hat{x} + y'\hat{y}$. The radiation pattern is being solve for and generally this is described in spherical coordinates, $\hat{r} = \hat{x}\sin\Theta\cos\Phi + \hat{y}\sin\Theta\sin\Phi + \hat{z}\cos\Theta$ [5]. Applying these coordinate systems to the quantity in the exponential yields $\hat{r}\cdot r' = x'\sin\Theta\cos\Phi + y'\sin\Theta\sin\Phi$. So the electric vector potential becomes

(2.10).

$$\vec{F} = \hat{y}E_o\epsilon\frac{exp(-j\beta r)}{4\pi r}\int\int_{Sa} exp(j\beta(x'\sin\Theta\cos\Phi + y'\sin\Theta\sin\Phi))dS' \tag{2.10}$$

Now the limits of the integration can be entered into the equation and the integral solved. The slot exists on the xy-plane so the surface integral will be over x and y. The length of the slot, s, is known to be approximately the thickness of the substrate. The width of the slot is the same as the width of the patch antenna, W.

$$\vec{F} = \hat{y}E_o\epsilon\frac{exp(-j\beta r)}{4\pi r}\int_{-W/2}^{W/2}\int_{-s/2}^{s/2} exp(j\beta(x'\sin\Theta\cos\Phi + y'\sin\Theta\sin\Phi))dx'dy' \tag{2.11}$$

$$\vec{F} = \hat{y}E_o\epsilon\frac{exp(-j\beta r)}{4\pi r}Ws\frac{\sin(\frac{\beta s}{2}\sin\Theta\cos\Phi)}{\frac{\beta s}{2}\sin\Theta\cos\Phi}\frac{\sin(\frac{\beta W}{2}\sin\Theta\sin\Phi)}{\frac{\beta W}{2}\sin\Theta\sin\Phi} \tag{2.12}$$

Since s is much smaller than a wavelength and if the new variable u is set to equal $\sin\Theta\cos\Phi$ the first fraction term from the integral equation can fit the form of (2.13) [15].

$$\lim_{v\to 0}\frac{\sin v}{v} = 1 \tag{2.13}$$

Using (2.13) on (2.12), and converting $\hat{y}$ to spherical coordinates, (2.14), the electric vector potential can be broken into Θ and Φ components, (2.15) and (2.16) respectively.

$$\hat{y} = \hat{r}\sin\Theta\sin\Phi + \hat{\Theta}\cos\Theta\sin\Phi + \hat{\Phi}\cos\Phi \tag{2.14}$$

$$F_\Theta = \cos\Theta\sin\Phi E_o\epsilon\frac{exp(-j\beta r)}{4\pi r}Ws\frac{\sin\left(\frac{\beta W}{2}\sin\Theta\sin\Phi\right)}{\frac{\beta W}{2}\sin\Theta\sin\Phi} \tag{2.15}$$

$$F_\Phi = \cos\Phi E_o\epsilon\frac{exp(-j\beta r)}{4\pi r}Ws\frac{\sin\left(\frac{\beta W}{2}\sin\Theta\sin\Phi\right)}{\frac{\beta W}{2}\sin\Theta\sin\Phi} \tag{2.16}$$

Now that the Θ and Φ components of the electric vector potential have been identified they can be used to find the magnetic field due to the electric vector potential, but not the entire magnetic field [13].

$$\vec{H_F} = -j\omega(F_\Theta\hat{\Theta} + F_\Phi\hat{\Phi}) \tag{2.17}$$

Since the radiation pattern is what is being solved for, the electromagnetic wave can be approximated as a plane wave. In that case the electric field associated with the electric vector potential can be related to the magnetic field associated with the electric vector potential [5].

$$\vec{E_F} = \eta H_F \times \hat{r} = -j\omega\eta(F_\Phi\hat{\Phi} - F_\Theta\hat{\Theta}) \tag{2.18}$$

Substitute (2.15) and (2.16) into (2.17)

$$\vec{E_F} = -j\epsilon\omega\eta E_o\frac{exp(-j\beta r)}{4\pi r}Ws\frac{\sin\left(\frac{\beta W}{2}\sin\Theta\sin\Phi\right)}{\frac{\beta W}{2}\sin\Theta\sin\Phi}(\cos\Phi\hat{\Theta} - \cos\Theta\sin\Phi\hat{\Phi}) \tag{2.19}$$

If the ground plane that lies in the xy-plane is assumed to be perfectly conducting image theory can be used to setup an equivalent but easier to solve problem. When the problem is mirrored across the xy-plane, the electric currents reverse in direction, and since the separation of the currents from the ground plane is very small, much less than a wavelength, the electric currents cancel each other out. This eliminates the need to solve for the magnetic vector potential. The magnetic currents do not reverse direction, so the magnetic currents add together doubling their magnitude [5]. So total electric field from a slot can be shown as

$$\vec{E_T} = 2\vec{E_F} = -j\epsilon\omega\eta E_o \frac{exp(-j\beta r)}{2\pi r} W s \frac{\sin\left(\frac{\beta W}{2}\sin\Theta\sin\Phi\right)}{\frac{\beta W}{2}\sin\Theta\sin\Phi}(\cos\Phi\hat{\Theta} - \cos\Theta\sin\Phi\hat{\Phi}) \tag{2.20}$$

From (2.20) the principle plane patterns can be found by setting Φ to 0^o for the E-plane and Φ to 90^o for the H-Plane. The normalized patterns are

$$G_{E-Plane}(\Theta) = 1 \tag{2.21}$$

$$G_{H-Plane}(\Theta) = \cos\Theta \frac{\sin(\frac{\beta W}{2}\sin\Theta)}{\frac{\beta W}{2}\sin\Theta} \tag{2.22}$$

Now that the pattern for a single slot has been solved for, array theory must be used to find the pattern from two slots. In order to find the array factor only the center points of the two slots will be considered. For the case of the H-Plane Pattern the points are always going to be equidistant so the energy received at any given point will be doubled. Since the radiation patterns are normalized this will have no effect on the H-plane pattern so

$$f_H(\Theta) = 1 \tag{2.23}$$

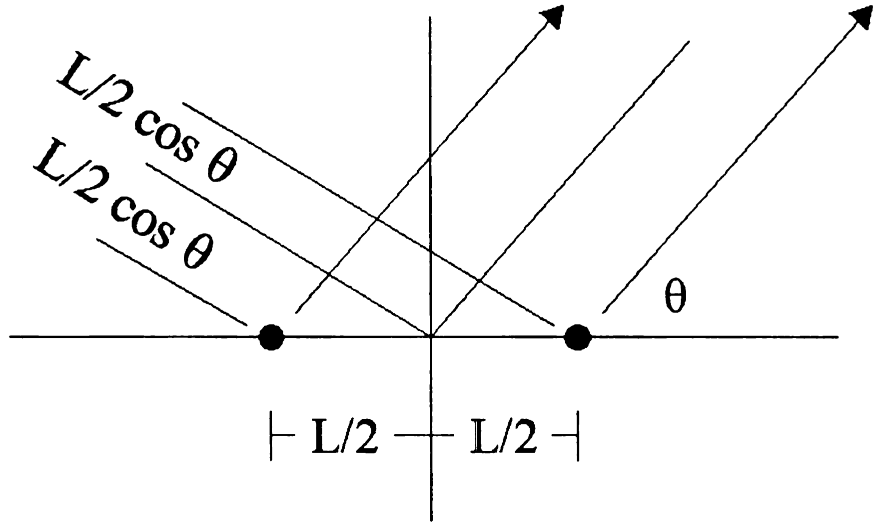

Figure 2.6. View of xz-plane with the dots representing centers of two slots.

The E-plane array factor is not as simple, as Figure 2.6 shows that any incoming wave that has oblique incidence will arrive at the each of the two points with a different phase. It can be seen that wave will arrive at the two points with a phase difference of $\pm L/2 \sin\Theta$ depending on the side of the origin the point is on. From this the array factor in the E-plane can be written as [7]

$$AF_E = exp(-j\beta(L/2)\sin\Theta) + exp(j\beta(L/2)\sin\Theta) = 2\cos(\beta\frac{L}{2}\sin\Theta). \tag{2.24}$$

After normalization the E-plane array factor is

$$f_E = \cos(\beta \frac{L}{2} \sin \Theta). \tag{2.25}$$

Using the E and H-plane array factors with the total electric field found in (2.21) and (2.22) the total fields of the array can be found.

$$F_E(\Theta) = G_{E-Plane}(\Theta) f_E(\Theta) = \cos(\beta \frac{L}{2} \sin \Theta) \tag{2.26}$$

$$F_H(\Theta) = G_{H-Plane}(\Theta) f_H(\Theta) = \cos \Theta \frac{\sin(\frac{\beta W}{2} \sin \Theta)}{\frac{\beta W}{2} \sin \Theta} \tag{2.27}$$

The fields found by (2.26) and (2.27) both have direct dependence on cosine of the angle Θ. So when the cosine term is maximized the pattern will be at a maximum. This occurs at $\Theta = 0$, along the z-axis. This is shown in Figures 2.7 and 2.8.

The theory behind patch antennas and microstrip has been presented in this chapter. Chapter 3 will introduce some methods of increasing the bandwidth of microstrip patch antennas and identify the an antenna type that will be further investigated through simulations.

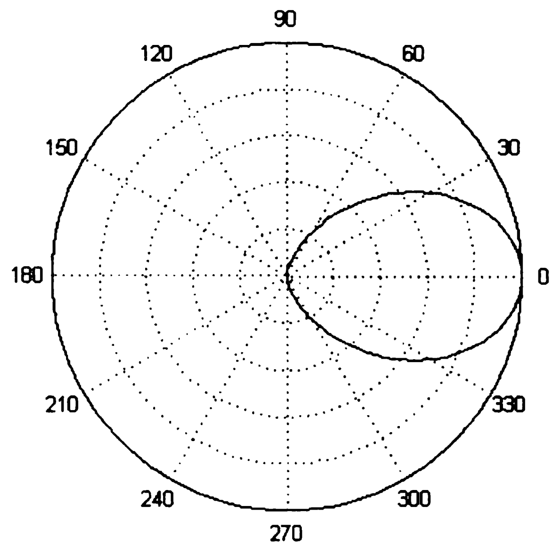

Figure 2.7. E-plane patch antenna pattern from theory.

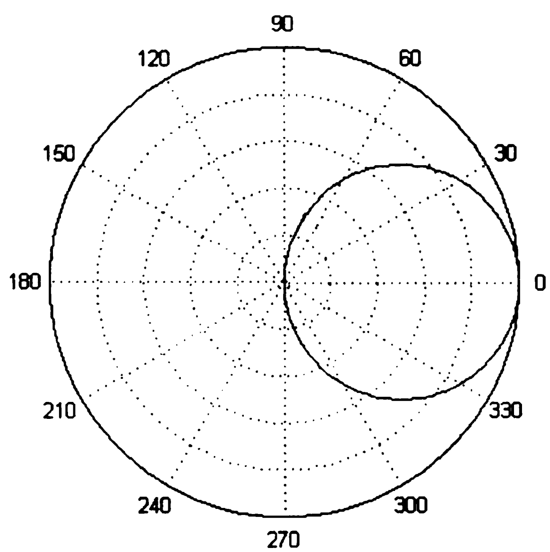

Figure 2.8. H-plane patch antenna pattern from theory.

CHAPTER 3

WIDEBAND PATCH ANTENNA DESIGN

As was discussed in the last chapter microstrip patch antennas share several properties with resonant cavities, most importantly they are resonant for only a very limited range of frequencies. This chapter will show several methods of increasing the bandwidth of patch antennas and describe the approach that was used to design a patch antenna meeting the bandwidth requirements for the Mini-UAV radar system.

3.1 Increasing Patch Antenna Bandwidth

Various way to increase the bandwidth of patch antennas have been researched. This section will present a couple basic methods that are commonly used, more methods can be found in [14].

3.1.1 Effect of the Substrate

The substrate used to build the patch antenna is a major contributor to the operational bandwidth of the antenna. Below is an approximation showing the relationship of substrate dielectric constant, ϵ_r, and thickness, t, to the bandwidth, BW, of the antenna, assuming the thickness is much less than a wavelength, λ [6].

$$BW = 3.77\frac{\epsilon_r - 1}{\epsilon_r}\frac{W}{L}\frac{t}{\lambda} \tag{3.1}$$

Since the length, width, and wavelength of the antenna cannot be changed the only tunable parameters of a rectangular patch antenna are the dielectric constant and substrate thickness. The approximation suggests that a lower dielectric constant and a thicker substrate will results in a wider bandwidth. In practical conditions using a square microstrip antenna with a teflon substrate with a dielectric constant of 2.2 and a thickness where $t/\lambda = 0.02$, the maximum bandwidth that can be expected is about 2%, much less than what is required for the Mini-UAV radar.

The thickness of the substrate could be increased to improve bandwidth, but there are undesirable effects when doing this. A thicker substrate allows higher order modes to form under the patch degrading the radiation patterns, efficiency, and polarization characteristics. The thicker substrates also lead to increased radiation from the microstrip feed line [14]. While the structural methods of increasing bandwidth are important and will be implemented, other methods of increasing bandwidth without having adverse effects on the antenna's other characteristics are required.

3.1.2 Effect of Coupled Feeds and Elements

Another method for increasing the bandwidth of a patch antenna is to have the patch fed through a coupled feed. Such a feed design will require two separate slabs of substrate. As shown in Figure 3.1, the top of the upper slab will have the patch(solid line), the feed line will sandwiched between the two slabs of substrate (broken line), and the bottom of the lower slab will be the ground plane. The feed line will extend underneath the patch by a distance S.

This feed configuration allows for several additional tunable parameters. There is now an additional slab of substrate where the thickness and dielectric constant can differ from the first slab. Also, the length that the feed line extends underneath the

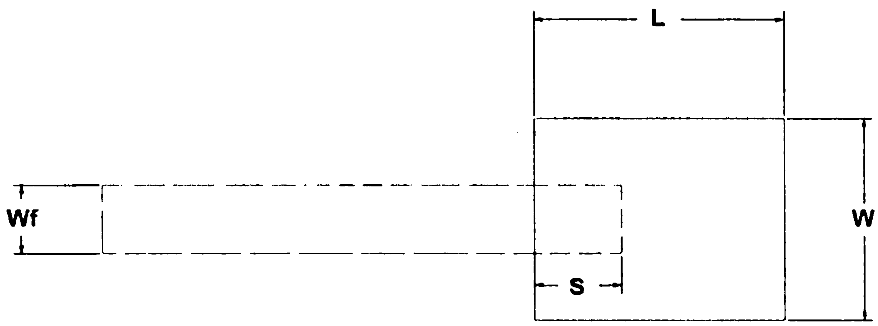

Figure 3.1. The geometry of a patch fed by a coupled feed.

patch, S, can be tuned. The lower substrate can be selected for optimum microstrip transmission line performance, thinner and higher dielectric constant. While the upper slab can be selected for optimum antenna performance, thicker with a lower dielectric constant. The length the feed line extends under the patch has an effect on the reactance of the antenna input impedance, by varying the length of overlap the impedance loop on the smith chart can be moved. For the best impedance match over a certain bandwidth the largest number of frequency points as possible should be as close as possible to the center of the smith chart [14].

Additional techniques for increasing bandwidth also exist. A stub can be placed on the side of the feedline, the stub then acts and a capacitor in series with the patch antenna. Adjustments to the side stub and the length that the feedline extends underneath the patch can yield bandwidths as high as 20%. This increased bandwidth comes at price of detriorated polarization characteristics and efficiency, since the side stub acts as a radiating elements interfering with the patch's radiation [14].

Coupling between antenna elements can also be used to increase the bandwidth of the antenna. This approach looks at patches as coupled resonators which can be tuned for wideband operation using circuit theory. The impedance of the antenna can be optimized by adjusting the spacing between elements, similar to the optimization done to the length of the feedline discussed previously. Antenna elements can be arranged in the same plane or stacked vertically.

The Mini-UAV requires a low profile antenna, so it would be desirable to use the planar coupled patches. Unfortunately in this configuration the feed network quickly becomes overly complex interfering with the antenna characteristics. Another draw back of the planar patches is that the coupling is generally weak between patches which results in narrower bandwidth. The patches can also be stacked vertically in order to keep the feed network simple. The patches are separated by a slab of substrate between each other. The thickness of this substrate provides another tunable parameter. These stacked patches have a couple significant draw backs. The biggest draw back of the vertical configuration is that the antenna is going to be taller than a planar configuration, the taller antenna also requires more material increasing the cost of the antenna [14].

3.2 Broadbanding Method Selection

The previous section showed methods of increasing bandwidth of patch antennas, however no single way was capable of providing the required bandwidth while maintaining a consistent pattern and polarization while meeting weight, ease of fabrication, and cost requirements. In [8] a microstrip patch antenna is presented that maintains a consistent pattern and polarization throughout a bandwidth as high as 25%. The antenna is also light and relatively simple to fabricate requiring only two layers of dielecric material and no vertical vias. This antenna design primarily employs the coupled element method of increasing bandwdith, but substrate selection still plays an important role in the antenna design.

Legay's stacked microstrip antenna combines the methods of increasing bandwidth described above into a single antenna design. The result is an antenna that has the low profile of planar patches and the higher coupling and bandwidth of vertically stacked patches. The general geometry of the antenna design is shown in Figure 3.2. The lower level of conducting material(broken line) is between the two layers of dielectric material. This level contained a microstrip line feeding a patch. The upper level of conducting material(solid lines) contains four patches centered above the driven patch on the lower level, these four patches are fed by coupling with the corners of the driven patch. Due to the adjacent resonant modes excited on the coupled patches and a broadbanding effect is realized [8].

It can be seen in Figure 3.2 that there are many parameters that can be tuned to obtained the desired antenna characteristics. $L1$ and $W1$ are the lengths and widths of the upper patches. $L2$ and $W2$ are the length and width of the lower patch. S_x and S_y are the distances between patches in both and x and y directions. The heights of the two substrates can also be tuned for optimal bandwidth. The width of the microstrip line, Wf, will depend on the thicknesses and dielectric constants of the substrates.

This antenna design offers all the properties required for the Mini-UAV radar

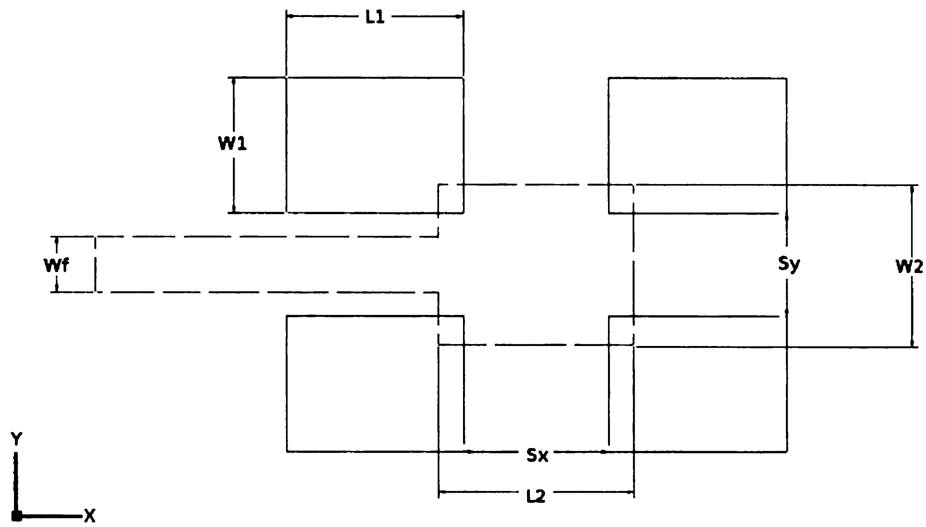

Figure 3.2. The geometry of Legay's stacked microstrip antenna.

system, bandwidths as high as 25%, linear polarization, single lobe radiation pattern, low profile, light weight, low material cost, and relatively simple fabrication. The antenna that was presented in [8] was designed to operate with a center frequency of 4.3 GHz, in order to use this type of antenna with the Mini-UAV radar system it must be redeisgned to operate at 12.5 GHz. To do this the antenna design will be scaled down in size. Table 3.1 shows the dimensions used in [8] and the resulting scaled dimensions. The dimensions were scaled by determining the ratio of the wavelengths of the two center freqeuncies ($24mm/70mm \approx 34\%$) and reducing the dimensions accordingly. These scaled values will be used only as approximate starting points, they will need to be further tuned because a different substrate material will be used for the Mini-UAV antenna.

Dimension	Orginal	Scaled
Frequency	4.3 GHz	12.5GHz
Wavelength	69.8mm	24mm
L1	20mm	6.88mm
W1	16mm	5.50mm
L2	21.3mm	7.32mm
W2	20mm	6.88mm
Sx	16mm	5.5mm
Sy	16mm	5.5mm

Table 3.1. Original and scaled antenna dimensions.

3.3 Material Selection

Before the antenna design process can proceed any further the materials that will be used as substrates must be selected. In order to keep the construction simple the same type and thickness of material will be used for both layers of substrate. One of the requirements of the substrate material is that it should be flexible enough to bend back about 90^o to connect the transmission line feeds to the RF sources of the radar system.

Originally Rogers 3003, a ceramic-filled polytetrafluoroethylene (PTFE, Teflon), was selected because of it it its high flexibility and acceptable dielectric constant of 3 [11]. Unfortunately, the 3003 was not easily machine by an inexperienced operator. In order to continue antenna design and testing an easier to machine material with comparable electrical properties was selected, Rogers 4003. This material is a glass reinforced hydrocarbon/ceramic laminate so it is not as flexible as the 3003, it also has a higher dielectric constant of 3.5 [12]. The higher dielectric constant is not desirable for a large bandwidth bandwidth antenna, but if an antenna can be designed to meet the bandwidth requirements with a higher dielectric constant material it can be tuned to operate with at least as large of a bandwidth using a material with a lower dielectric constant. This is the material that will be used for the rest of the design, simulation, fabrication, and testing stages. If it proves to be too rigid redesigning the antenna with a slightly lower dielectric substrate will not be difficult.

A thickness of substrate material also needs to be selected. Rogers 4003 comes in several standard thicknesses. As was shown earlier a thicker substrate has better broadbanding effects. The thickest 4003 is readily available is 1.524mm (60mil), however when two pieces of this thickness are stacked they the total thickness is no longer much smaller than a wavelength, 2.4mm, so multiple modes will form producing undesirable effects. The next step down has a thickness of 0.813mm (32 mil), when stacked this material is much smaller than a wavelength [12]. Also, Rogers 3003 is available in a thickness of 0.75mm (30 mil), so the thickness would not have a large change if 3003 is required in the future [11].

Now that an antenna type that can meet the antenna requirements has been identified, a design starting point has been made by scaling the original antenna design, and a substrate has been selected the antenna tuning process can begin. The antenna tuning will be performed primarily through simulations that will be discussed in detail in Chapter 4.

CHAPTER 4

WIDEBAND PATCH ANTENNA SIMULATIONS

In the previous chapter, Chapter 3, a possible antenna design was identified, it was also noted that due to changes in substrate material that simply scaling the antenna design would not produce a good antenna design and additional tuning would be required. This chapter will discuss how this tuning was accomplished using Ansoft Corporation's High Frequency Structural Simulator (HFSS). The tunable parameters of the antenna will also be identified and their effects on the antenna's electrical properties will be shown. At the end of this chapter the dimensions of an antenna capable of meeting the Mini-UAV requirements will be presented.

4.1 HFSS Simulation Setup

Ansoft's HFSS uses the finite element method (FEM) to provide full wave electromagnetic solutions to three dimensional geometries [2]. To use HFSS a three dimensional model of the geometry that needs to be simulated must be drawn. Each three dimensional object in the model must also be assigned material properties such as permittivity, loss tangent, and permeability. Once the model is drawn and the material properties are assigned, HFSS creates a mesh of the model using basic geometric shapes, usually triangles. FEM is then used to solve for the fields at the surfaces of the modeled objects using the boundary conditions that are dependent on material properties. The results from these calculations can then provide important information such as port impedance, which can also be interpreted as VSWR, smith charts, and return loss, and radiations patterns. Observations of both port impedance and radiation patterns will be used to evaluate each iteration of the antenna design

4.1.1 Drawing the Antenna Geometry

The completed drawing of the antenna geometry can be seen in Figure 4.1. This section will detail the steps taken to create the drawing. First a volume must be defined in which the fields will be calculated. In this situation where, apart from the antenna and its feed, everything is either freespace or ground plane, so a boundary box can be constructed around where the antenna will be drawn. The bottom of the box will be set to have an infinite ground plane boundary condition, the remaining 5 sides will be configured as radiation boundaries acting as perfectly absorbing material. The dimensions of the boundary box used for this simulation were chosen to be 26.67mm x 26.67mm x 17.5mm, a volume large enough for the entire antenna to fit inside. The bottom of the boundary box will be on the $z = 0$ plane, the top will be on the $z = 17.5mm$ plane. The box will also be centered at the origin of the xy-plane

Once the volume where the fields will be solved is defined, the various components of the antenna can be drawn. Starting from the bottom the first component will be a copper ground plane. The copper ground plane needs to cover the entire bottom of the box, so it will be a 26.67mm square. A thickness of $35\mu m$ will used for the copper, this is equivalent to a $1oz/ft^2$ copper cladding that is commonly available on dielectric materials. The copper square will be given the material properties of copper in HFSS. The next component on the stack is the bottom slab for substrate material, this also needs to entirely cover the ground plane so it is also a 26.67mm

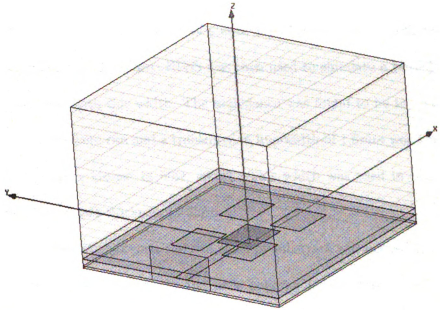

Figure 4.1. The antenna geometry drawn in HFSS.

square. The substrate thickness was decided in Chapter 3 to be $0.81mm$. The slab is assign a dielectric constant of 3.5.

The transmission line feed and driven patch are placed on top of the bottom slab of substrate. The $L2$ and $W2$ from Chapter 3 are used as the dimensions of the driven patch. The thickness and material properties of the copper patch and transmission line are the same as the ground plane, $35\mu m$. The transmission line is chosen to extend from the narrow edge of the driven patch on the negative x side to the edge of the box on the negative x side. The width of the transmission line has not been calculated yet.

The equations from Chapter 2, (2.1), (2.2), and (2.3), can be used as a guideline, but since the the transmission line is buried between two slabs of dielectric with air on top of the upper slab the equations will not produce an accurate width. The equations determine that the width of a uncovered 50Ω transmission line on $0.81mm$ Rogers 4003 should be $1.8mm$. HFSS was then used to simulate a buried microstrip transmission line with this width. The impedance was found to be too low, a couple more simulations were run and a transmission line width of $1.6mm$ was found to have have an impedance closest to 50Ω, 49.2Ω. This width was used in the simulation along with the copper thickness of $35\mu m$.

When building the antenna the two slabs of substrate will needed to be bonded, this is accomplished through the use of a bonding film. More details about the bonding film will be presented in Chapter 5. For the simulation only the thickness and dielectric constant are required. The bonding film that will be used for bonding the substrates is Rogers 3001, it has a thickness of $0.0381mm$ and a dielectric constant of 2.28 [10]. The bonding film is also $26.67mm$ square.

The upper slab of substrate is the next component to be added to the stack, this slab is identical in dimensions and properties to the bottom slab. The final layer of the antenna stack contains the four top patches. The general layout of the four patches in relation to the driven patch can be seen in Figure 3.2. The values for $L1$, $W1$, Sx, and Sy are taken from Table 3.1. The thickness for this layer of copper is the same as the other copper layer, $35\mu m$.

The simulation is now almost ready to run, the last step is to setup an excitation port. To do this a rectangle needs to be drawn on the side of the boundary box that the transmission line touches, this will be the port where a signal would be connected to the antenna. The port will be centered at $y = 0$ and have a width of five times the width of the transmission line. In the z-direction port will extend from the top of the ground plane to a height of five times the thickness of the lower slab of substrate. The port must be this large to allow a realistic field structure to setup around the transmission line.

4.2 Simulating the Scaled Antenna

While it has already been stated that due to changes in the substrate material the scaled antenna would not have desirable performance, this section will present some results of the simulation of the scaled antenna to show that tuning does in fact need to be performed. The simulation is run from $10GHz$ to $14GHz$ so the entire range of frequencies the antenna needs operate is will be covered.

4.2.1 Port Impedance

The first plot, shown in Figure 4.2, displays the return loss of the antenna, or S11. The return loss is a direct measurement of how much of the energy that is sent into a device is returned to the source. In a short circuit all the energy is returned to the source, a return loss of $0dB$. A perfectly matched matched source would have no energy returned to the source. In reality this is not possible, but a return loss of $-40dB$ (1% of the energy returned) is considered good. This information can be useful in determining what frequency the antenna is resonant/radiates. A low S11 corresponds to less energy being reflected back to the source. In the case of an antenna constructed out of low loss material the majority of the energy is going to be radiated out into space at frequencies with a low return loss.

Figure 4.2 shows that there is a large and narrow dip in the return loss around

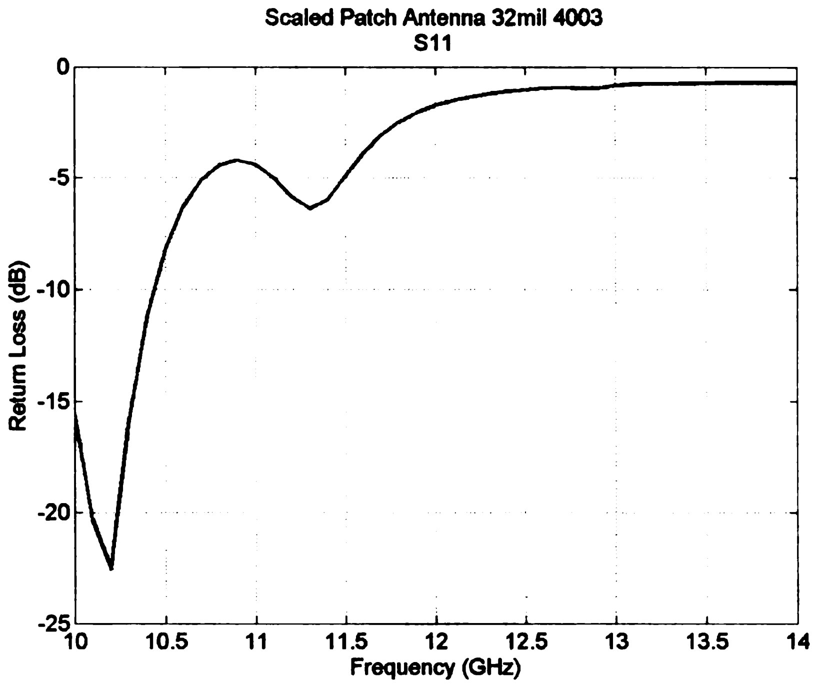

Figure 4.2. Return loss of the simulated scaled antenna.

$10.2GHz$. This means that the antenna will radiate best at $10.2GHz$, out of the range required by the Mini-UAV. The narrow dip corresponds to a narrow bandwidth.

Often VSWR plots are used to show the bandwidth of an antenna. The lower VSWR, the better the match between the antenna and source. A better match results in more energy being radiated from the antenna and less energy be reflected back to the source. Generally a VSWR of less than 2 is considered acceptable for most applications, this corresponds to a return loss of about -9.54 dB or less. VSWR can be calculated from S11 by (4.1).

$$VSWR = \frac{1 + 10^{(-S11/20)}}{1 - 10^{(-S11/20)}} \tag{4.1}$$

The VSWR of the scaled antenna is shown in Figure 4.3. The vertical line in Figure 4.3 represents a VSWR of 2. Frequencies where the VSWR is below this line are where the antenna will be well matched with the antenna. Based on the range of frequencies where the VSWR is below 2 the bandwidth of the antenna can be calculated from (4.2). To find the bandwidth percentage, the center frequency of the bandwidth must also be calculated, (4.3). Using bandwidth and center frequency the bandwidth can be calculated, (4.4).

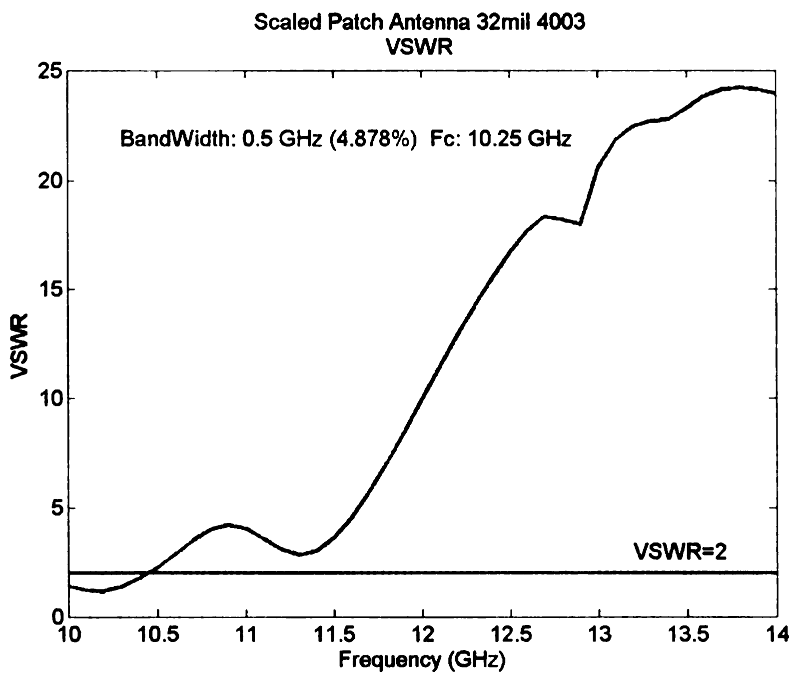

Figure 4.3. VSWR of the simulated scaled antenna.

$$Bandwidth = HighCrossingPoint - LowCrossingPoint \tag{4.2}$$

$$CenterFrequency = \frac{Bandwidth}{2} + LowCrossingPoint \tag{4.3}$$

$$Bandwidth\% = \frac{Bandwidth}{CenterFrequency} \tag{4.4}$$

The results of these calculations are shown in Figure 4.3. The bandwidth is $500MHz$ (5%) centered at $10.25GHz$. This only considers the frequencies from $10GHz$ and up. Since $10.5GHz$, the highest frequency with a VSWR less than 2, is already still well below the frequency range of interest for this antenna, it can be concluded that this design will not operate well in the required frequency range.

Another way to interpret the port impedance data is the smith chart. The smith chart allows both the real and imaginary components of the input impedance of the antenna to be plotted on a grid. The smith chart has many uses, however when trying to match the antenna with the source impedance it can generally be stated that as many frequency points as possible should be as close as possible to the center of the chart. The center of the chart represents a perfect match to the reference impedance, in this situation 50Ω. The real axis crosses the center of the circle from left to right. Points on the real axis to the left of center have a smaller real impedance than reference, to the right, larger. The areas above and below the real axis represent reactance, positive above and negative below. Figure 4.4 shows the smith chart data from the scaled antenna.

From Figure 4.3 it was noted that the antenna had the best impedance match at lower frequencies. This can be seen in Figure 4.4 as well, the lower frequency points start out near the center of the smith chart. As frequency increases however the

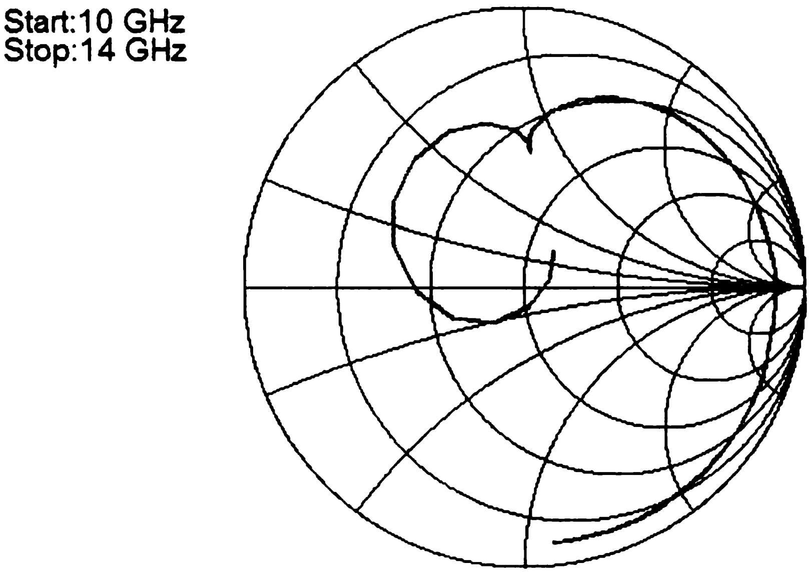

Figure 4.4. Smith chart showing the impedance of the simulated scaled antenna.

impedance of the antenna rapidly approaches the edges of the chart indicating a poor match. This was also shown in the return loss and VSWR plots, Figures 4.2 and 4.3.

4.2.2 Radiation Patterns

From the port impedance provided by the simulation it is known that this scaled antenna will not operate as desired in the frequency band of the Mini-UAV. Too much of the signal fed to the antenna will be reflected back to the source, reducing the amount that will be radiated. However, port impedance is not the only antenna parameter that needs to be considered, the radiation pattern of the antenna is also very important. HFSS is capable calculating the far-field radiation pattern of geometries it simulates.

Just because an antenna is radiating, does not mean that it is radiating equally in all directions. Every antenna has a radiation pattern that will be determined by how the electromagnetic fields behave in the geometry. In Chapter 2 the E-plane and H-plane of a single patch antenna was derived, it indicated that the patch would have a broadside pattern perpendicular to the plane of the patch. Since this antenna is also a patch antenna it should also have a broadside pattern. Unfortunately, as can be seen in Figures 4.5 and 4.6 the patterns of this antenna at $12GHz$ do not have a main beam, the maximum gain observed in either of the two patterns is only a fraction of a dB. As was stated previously the antenna is not well matched around $12GHz$ so not much energy is making it to the antenna to be radiated. From the

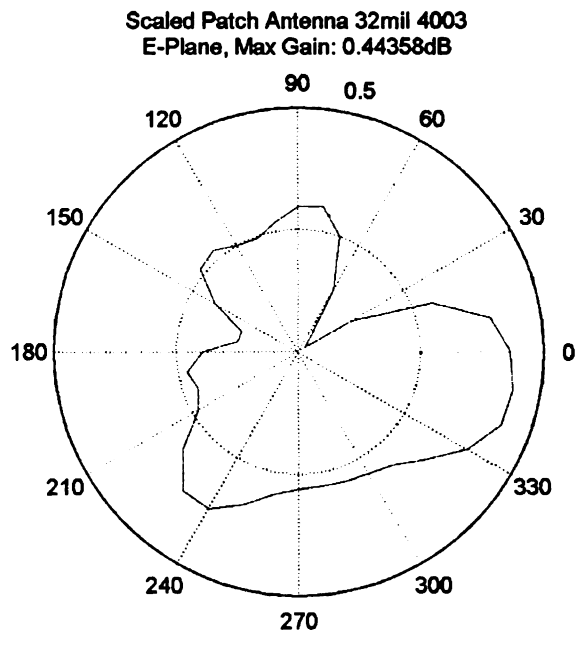

Figure 4.5. Simulated scaled antenna E-Plane pattern at 12GHz.

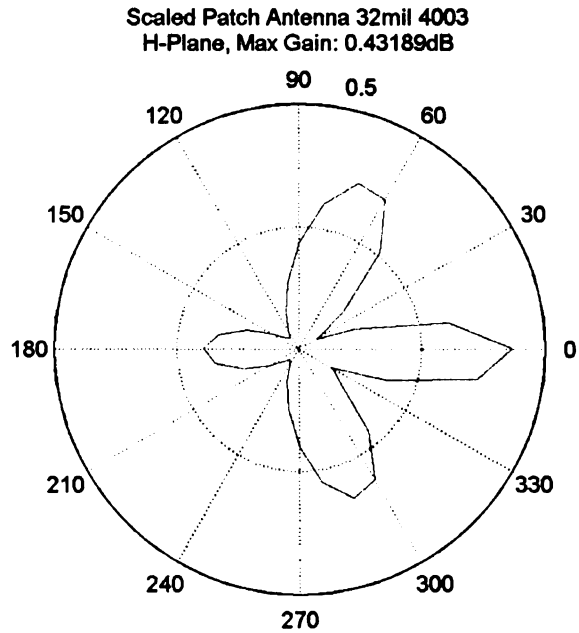

Figure 4.6. Simulated scaled antenna H-Plane pattern at 12GHz.

results of the simulation of the scaled antenna it can be seen that this antenna will not meet the performance requirements of the Mini-UAV radar system. This antenna will be used as a starting point and the various parameters of the antenna will be adjusted and the effects of these adjustments will be noted.

4.3 Antenna Tuning

In this section the various parameters of the antenna that can be tuned will be presented and the results of tuning certain parameters will be discussed. The only parameters that cannot be changes are the substrate height, substrate dielectric constant, and the width of the transmission line feed. The sizes of all the patches and the separation of the upper patches can all be adjusted. Many trials where performed using HFSS, and trends were found that allowed for a design process to be developed.

4.3.1 Frequency Adjustment

The operating frequency of the simulated scaled antenna was noted as being lower than desired. In Chapter 2 it was shown that the resonant frequency of a patch antenna depends primarily on the lengths of the radiating patches. For this antenna design the majority of the radiation comes from the top four patches. It can then be reasoned that by changing the lengths of the top four patches, $L1$, that the frequency the antenna operates at can be tuned. Figure 4.7 shows the VSWR of the simulated

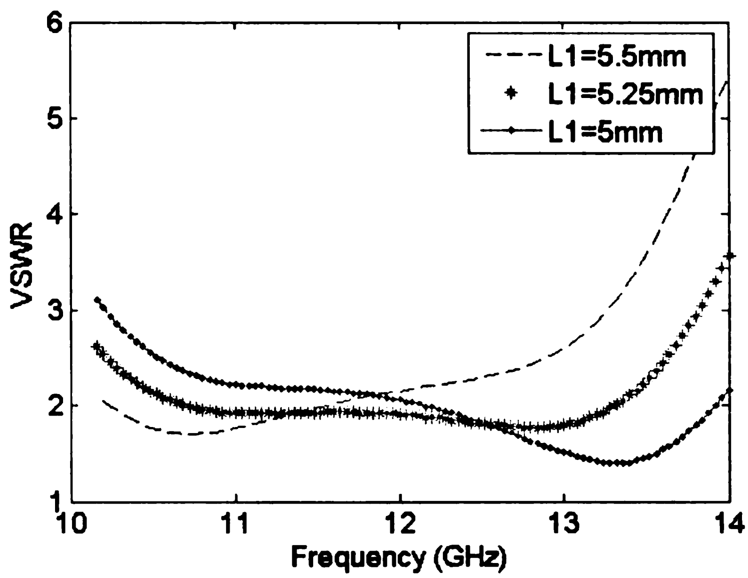

Figure 4.7. VSWR plots of simulated antennas with varying $L1$.

antennas with varying $L1$'s. As expected a larger $L1$ results in a better match at lower frequencies that have longer wavelengths. As $L1$ is decreased in size from 5.5mm to 5mm the best matched frequencies of the antenna increase from 10.7GHz to 13.2GHz.

4.3.2 Impedance Loop Size

The impedance loop that can be observed on smith charts is a result from antenna elements coupling together. As elements are closer together and they overlap the driven patch more they have a stronger coupling, this results in larger coupling loop on the smith chart. It was noticed that the y-spacing, Sy, had a much larger effect than the x-spacing, Sx. This suggest a stronger coupling in the y-direction. Figures 4.8 to 4.11 show the effects of increasing the y-spacing from from 2mm up to 3.5mm. As expected, the smaller spacings have larger impedance loop. It should also be noted that changes in the y-spacing have almost not effect on the position of the loop.

The effect of the loop size on VSWR is shown in Figures 4.12 to 4.15. When the impedance loop is larger (Figure 4.12) there are a greater number of frequency points around the center, however none of the points are very close to the center. There is no frequency where the VSWR is much less than 2. The smaller loops shown in Figure 4.14 and 4.15 have a narrower range of frequencies near the center, but the frequencies near the center are closer, resulting in a lower VSWR at those frequencies.

4.3.3 Impedance Loop Position

Apart from the changing the impedance loop size, the loop can be rotated. It has already been shown that the area that the upper patches overlap the driven patch controls the size of the impedance loop, if the overlap area is kept the same by

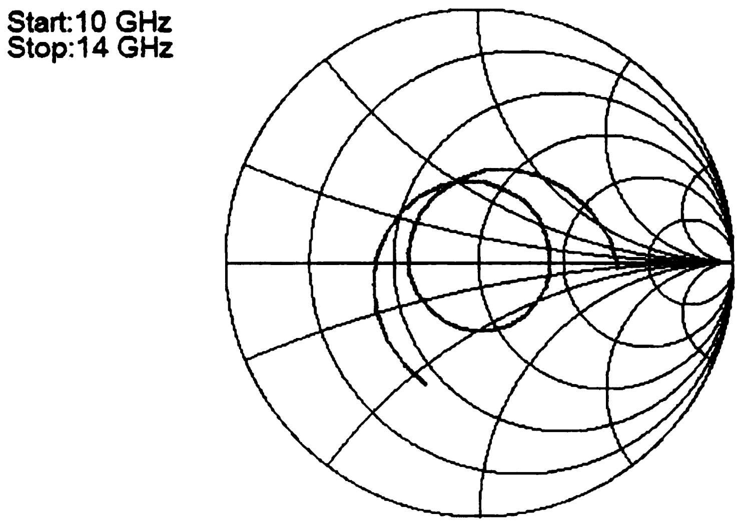

Figure 4.8. Smith Chart of a simulated antenna with y-spacing of $2mm$.

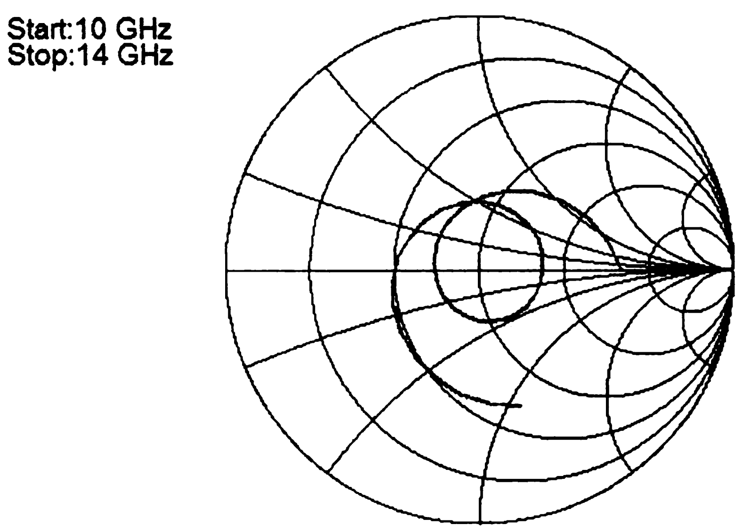

Figure 4.9. Smith Chart of a simulated antenna with y-spacing of $2.5mm$.

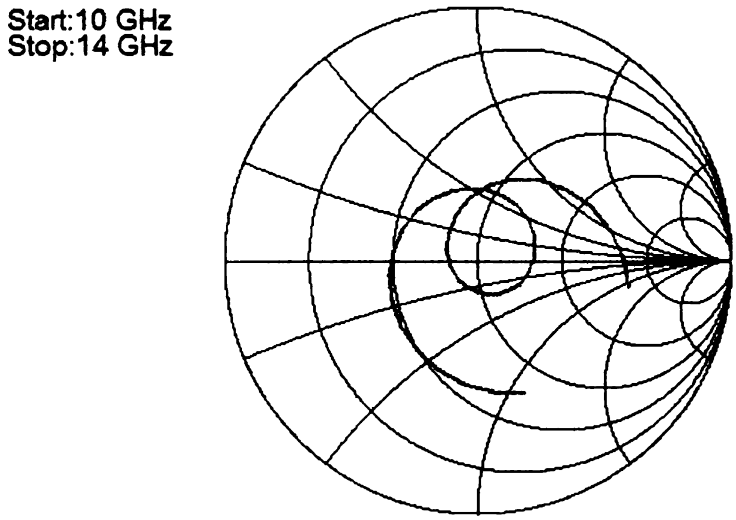

Figure 4.10. Smith Chart of a simulated antenna with y-spacing of $3mm$.

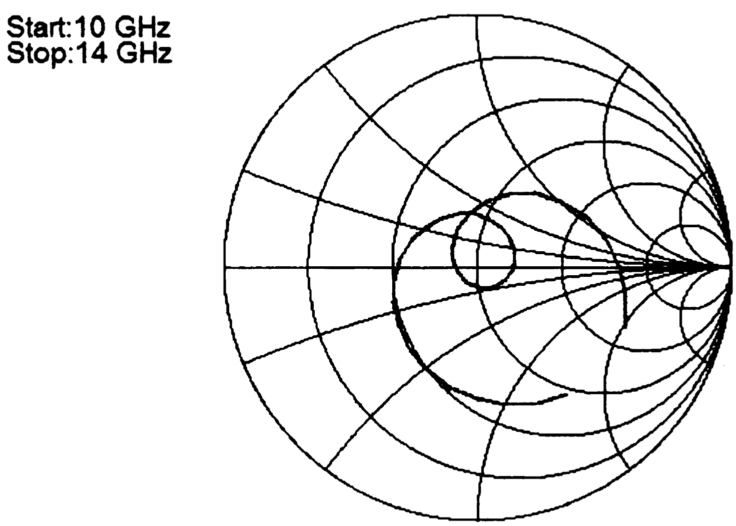

Figure 4.11. Smith Chart of a simulated antenna with y-spacing of $3.5mm$.

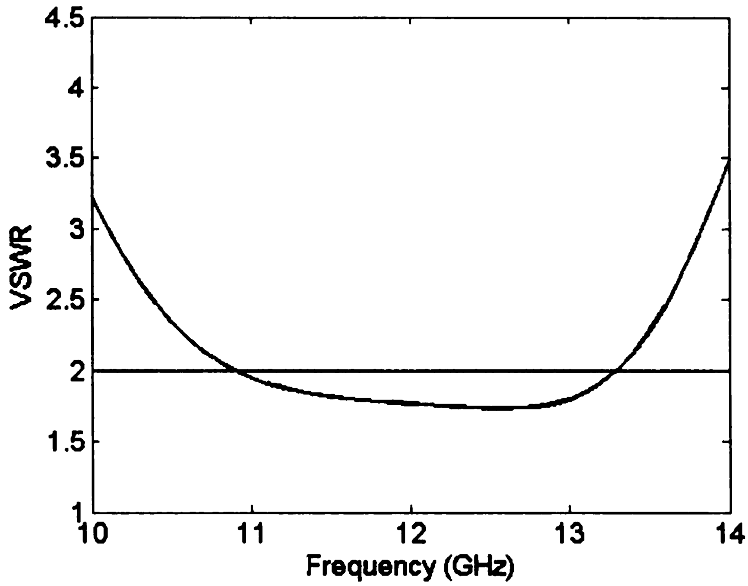

Figure 4.12. VSWR of a simulated antenna with y-spacing of $2mm$.

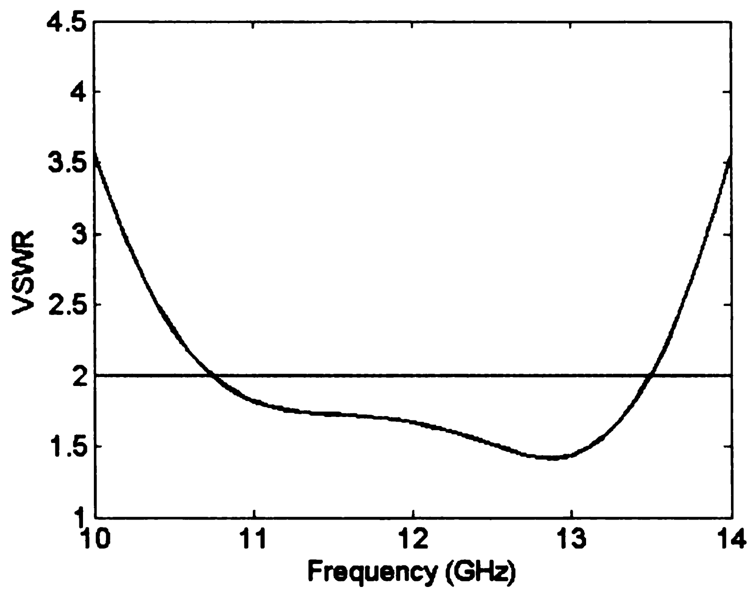

Figure 4.13. VSWR of a simulated antenna with y-spacing of $2.5mm$.

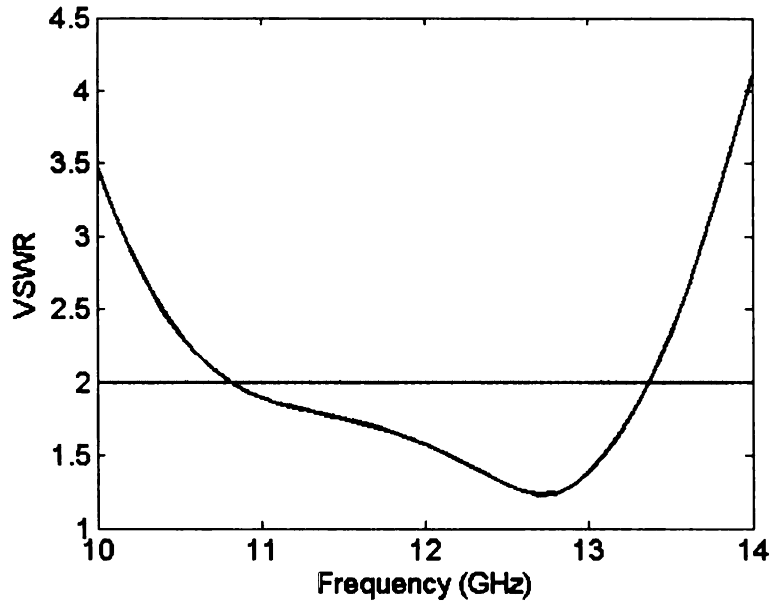

Figure 4.14. VSWR of a simulated antenna with y-spacing of $3mm$.

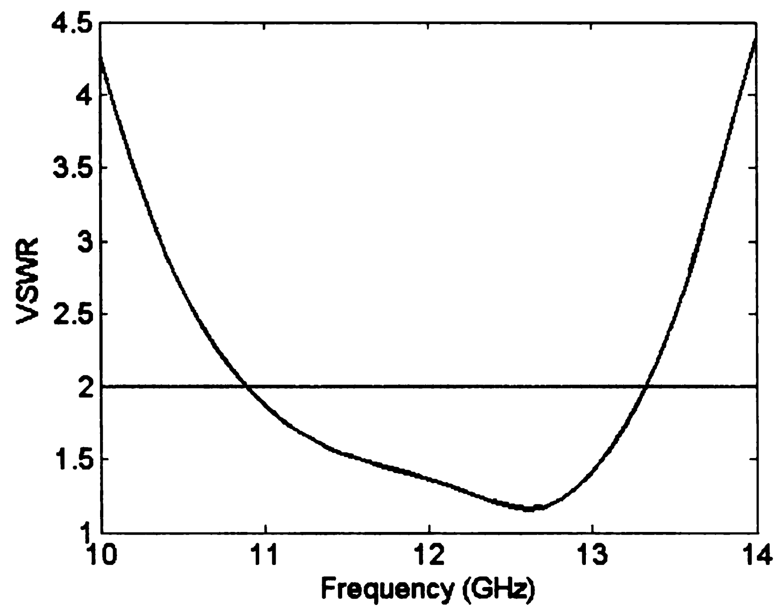

Figure 4.15. VSWR of a simulated antenna with y-spacing of $3.5mm$.

decreasing both the y-spacing and the width of the driven patch, $W2$, by the same amount that the loop will rotate the smith chart counter-clockwise. By adjusting the y-spacing and driven patch width the impedance loop can be moved to the center of the smith chart, resulting in a better impedance match. Figures 4.16 through 4.19 show the counter clockwise movement of the smith chart as the y-spacing and driven patch width is decreased.

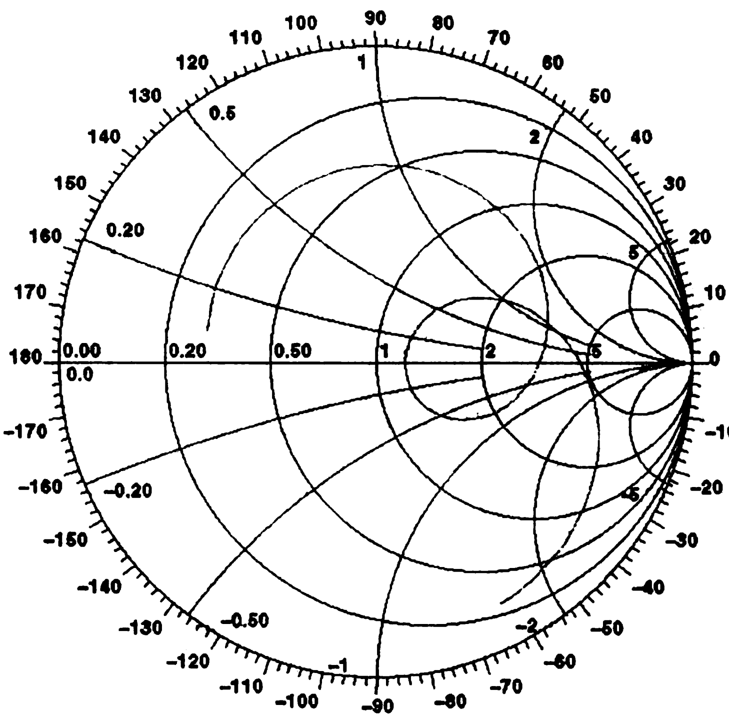

Figure 4.16. Smith chart of a simulated antenna with $Sy = 3.67mm$ and $W2 = 6.33$.

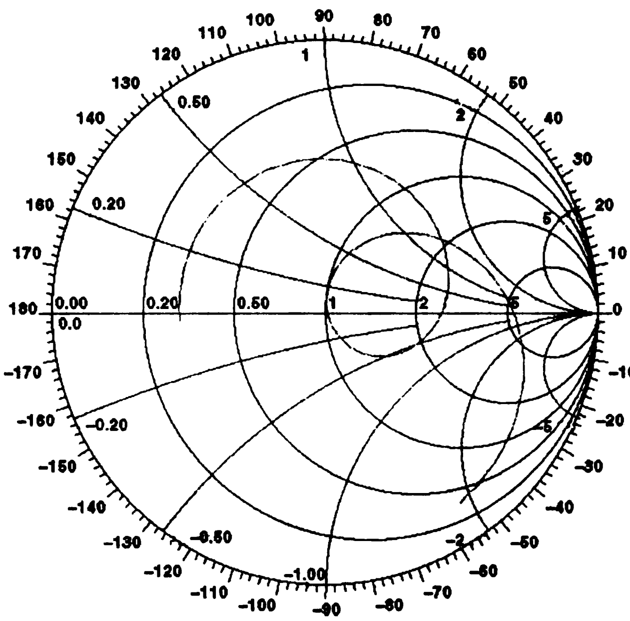

Figure 4.17. Smith chart of a simulated antenna with $Sy = 3mm$ and $W2 = 5.67$.

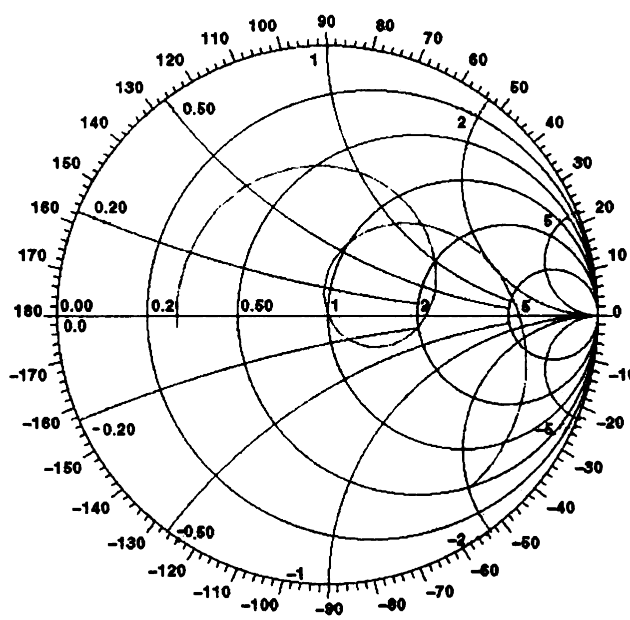

Figure 4.18. Smith chart of a simulated antenna with $Sy = 2.67mm$ and $W2 = 5.33$.

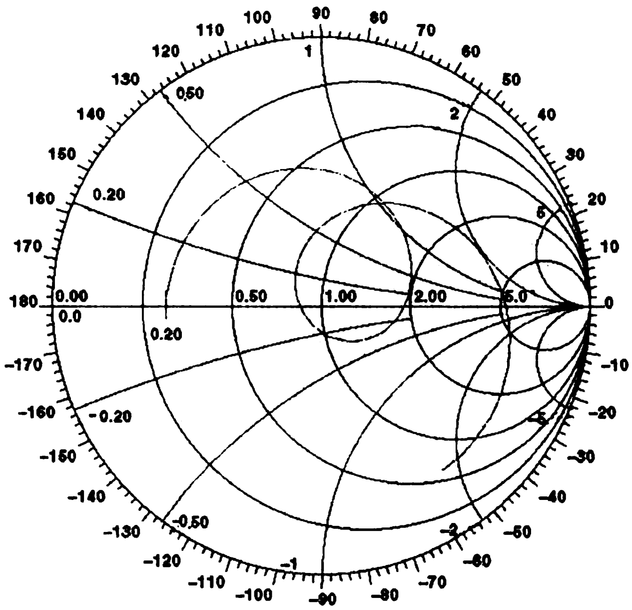

Figure 4.19. Smith chart of a simulated antenna with $Sy = 2mm$ and $W2 = 4.67$.

4.4 Tuned Antenna

Using the antenna tuning methods discussed above an antenna design that will potentially meet the criteria for the Mini-UAV was found. Below are the simulation results from the optimized antenna design. The dimensions of this antenna are shown in Table 4.1.

Dimension	Optimized Value
L1	5.2mm
W1	4mm
L2	5.75mm
W2	4.67mm
Sx	4.25mm
Sy	3mm

Table 4.1. Optimized antenna dimensions.

4.4.1 Simulated Impedance Results

Figure 4.20 shows the simulated return loss of the antenna. It indicates the best impedance match occurs around $12.6GHz$. Also, acceptable match, where the return loss is $-10dB$ or less, ranges from $11GHz$ to $13.3GHz$.

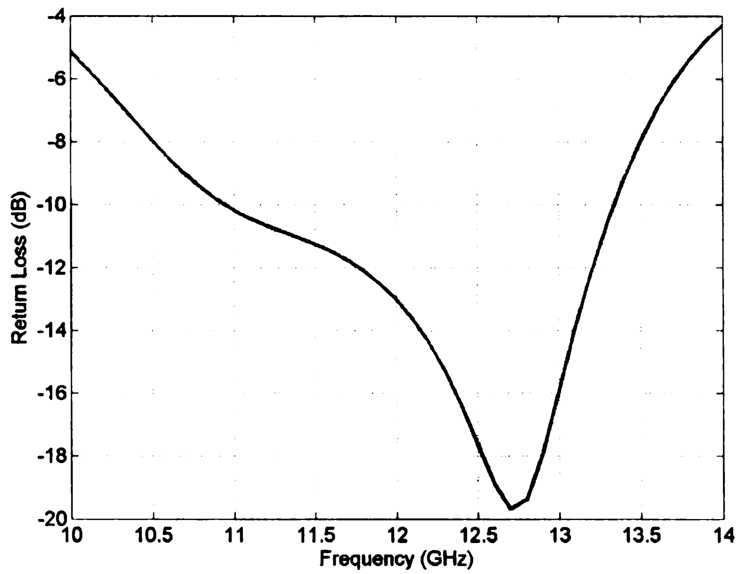

Figure 4.20. Return loss of simulated optimized antenna design.

The smith chart of the optimized design is shown in Figure 4.21. The impedance loop is located near the center and has a midrange size, to reach the best compromise of bandwidth and matching.

The VSWR of the design is presented in Figure 4.22. The simulation shows a VSWR of less than two from $10.7GHz$ and $13.3GHz$, 20.6% bandwidth.

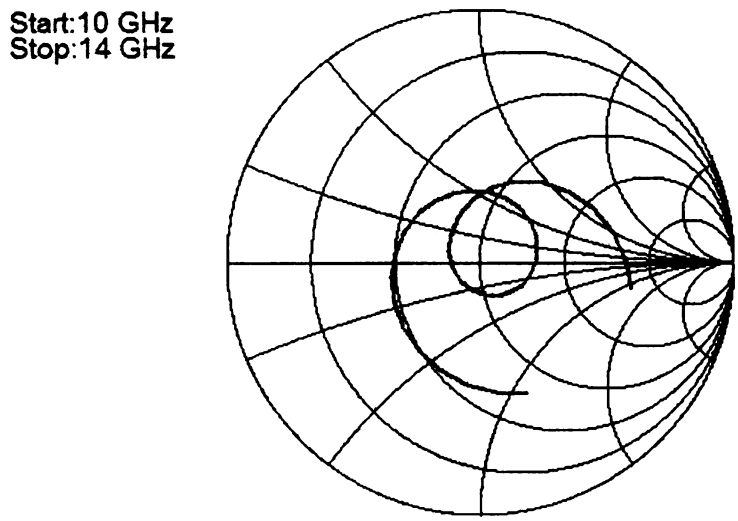

Figure 4.21. Smith Chart of simulated optimized antenna design.

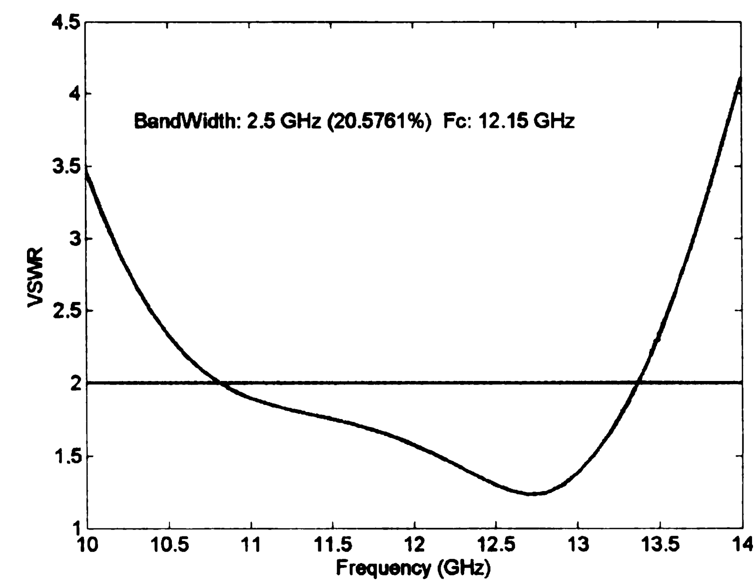

Figure 4.22. VSWR of simulated optimized antenna design.

4.4.2 Simulated Radiation Patterns

The simulated impedance results show the optimized antenna meets the bandwidth requirements of the Mini-UAV. The radiation patterns of the antenna should also be considered before the design is built and tested. Figures 4.23 to 4.28 show the E-plane fields of the simulated optimized antenna design at frequencies from $11GHz$ to $13.5GHZ$.

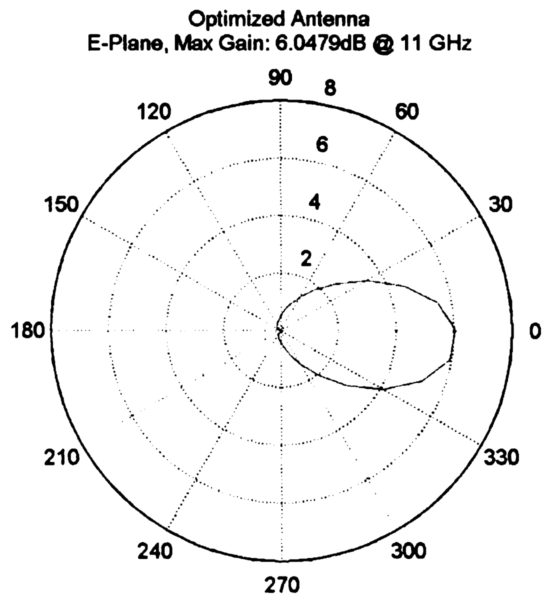

Figure 4.23. E-Plane Radiation pattern of simulated optimized antenna at $11GHz$.

In the E-plane the pattern of the antenna is a single broadside lobe at all frequencies. The beam shifts a few degrees through the frequency sweep, but the shifts are not large enough to be problematic. Since the transmission line feed is not symmetric

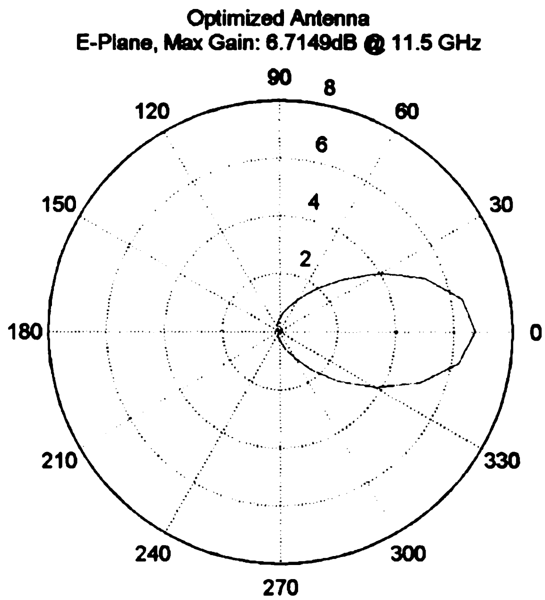

Figure 4.24. E-Plane Radiation pattern of simulated optimized antenna at $11.5GHz$.

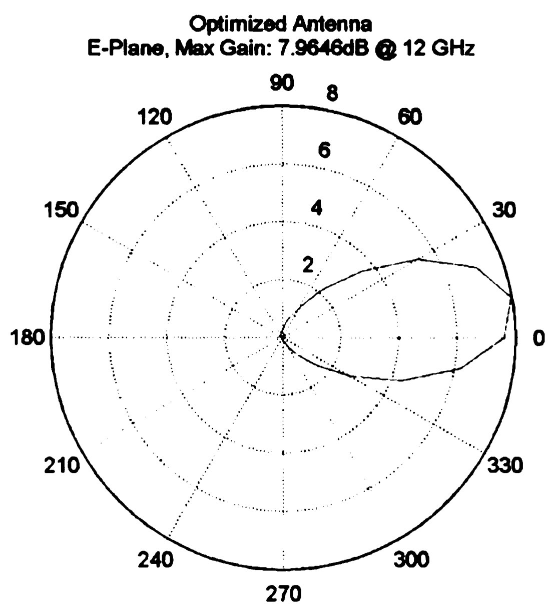

Figure 4.25. E-Plane Radiation pattern of simulated optimized antenna at $12GHz$.

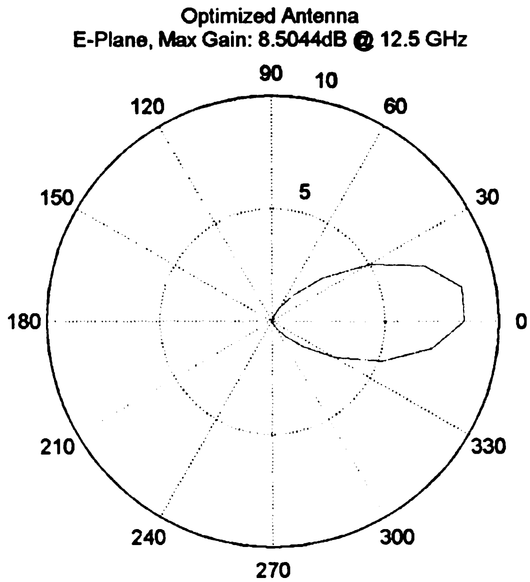

Figure 4.26. E-Plane Radiation pattern of simulated optimized antenna at $12.5GHz$.

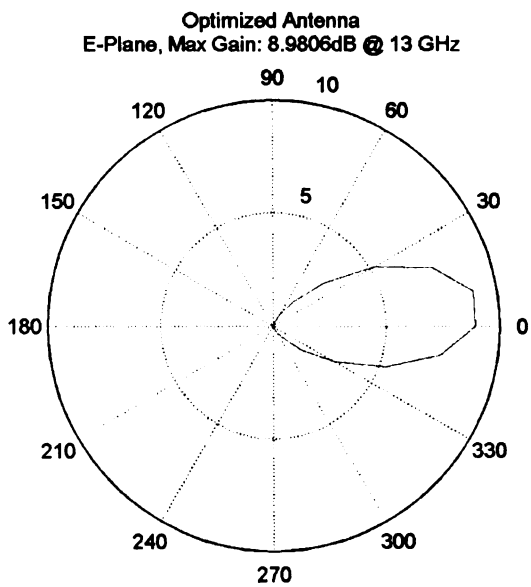

Figure 4.27. E-Plane Radiation pattern of simulated optimized antenna at $13GHz$.

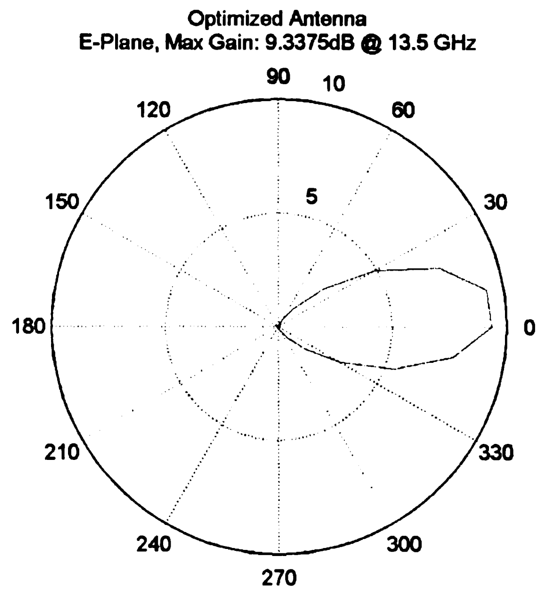

Figure 4.28. E-Plane Radiation pattern of simulated optimized antenna at $13.5GHz$.

in the E-plane, it contributes to the radiation pattern and causes the pattern shifts. The simulated gain of the antenna varies from $6dB$ to $9.3dB$.

Figures 4.29 to 4.34 show the H-plane pattern through the same frequency sweep. The contributions of the feedline are symmetric in the H-plane so main beam does not shift in the H-plane.

The simulation shows that the optimized design has radiation pattern that offers acceptable gain and shape through the entire bandwidth of the antenna. Based on the simulation results of the optimized antenna a prototype will be built. The fabrication and testing of the prototype are presented in Chapter 5.

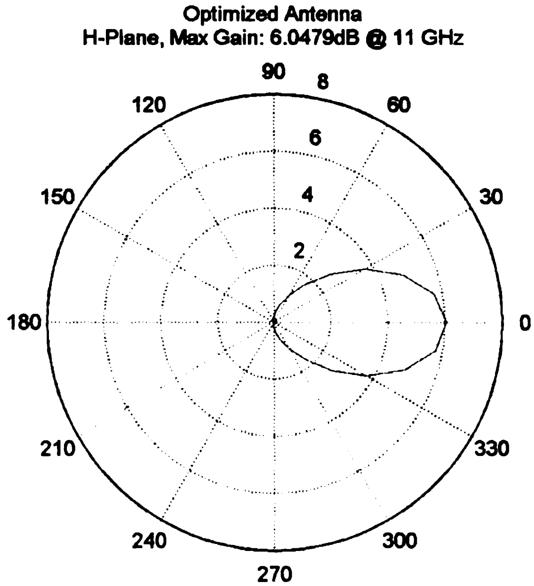

Figure 4.29. H-Plane Radiation pattern of simulated optimized antenna at $11GHz$.

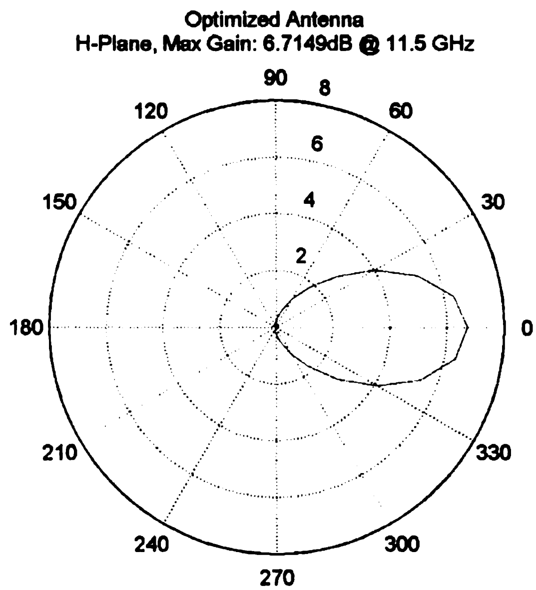

Figure 4.30. H-Plane Radiation pattern of simulated optimized antenna at $11.5GHz$.

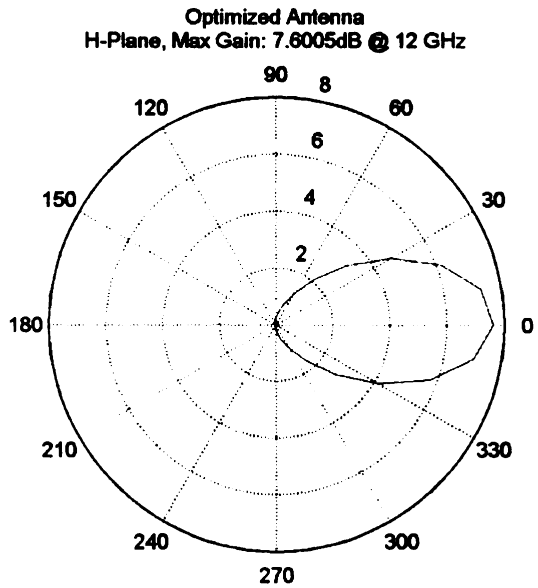

Figure 4.31. H-Plane Radiation pattern of simulated optimized antenna at $12GHz$.

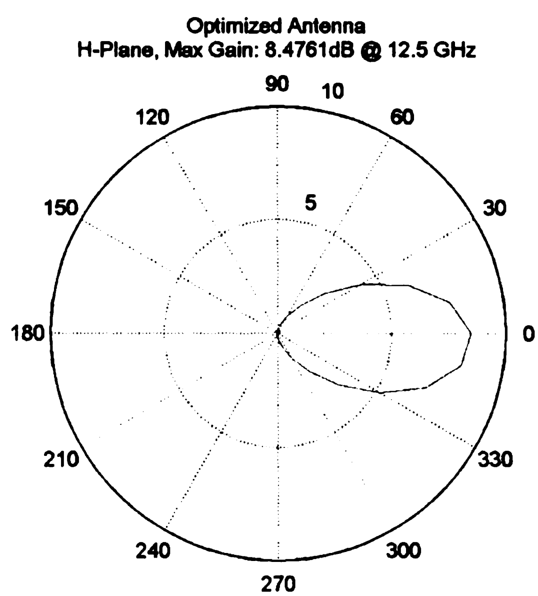

Figure 4.32. H-Plane Radiation pattern of simulated optimized antenna at $12.5GHz$.

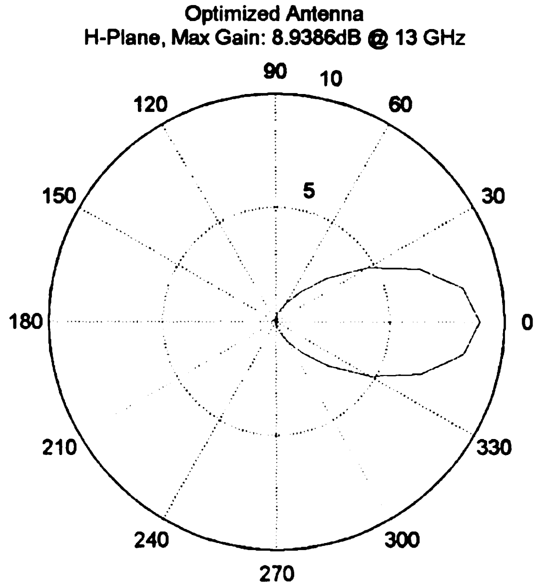

Figure 4.33. H-Plane Radiation pattern of simulated optimized antenna at $13GHz$.

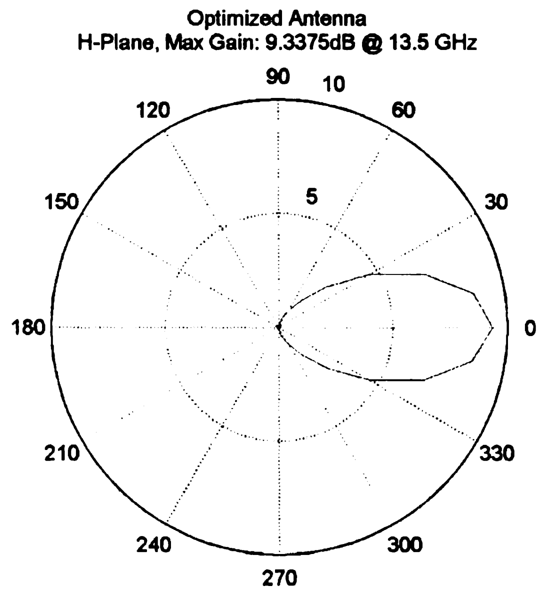

Figure 4.34. H-Plane Radiation pattern of simulated optimized antenna at $13.5GHz$.

CHAPTER 5

ANTENNA FABRICATION AND TESTING

Chapter 4 used simulations to arrive at an antenna design that will, in simulation, meet the requirements for the Mini-UAV radar system. To experimentally confirm the simulation results prototypes will be fabricated. Impedance and radiation pattern measurements will then we performed on the prototypes and the results compared to simulation. This chapter will describe the fabrication and measurement processes and present the experimental results.

5.1 Fabrication

The fabrication process starts with a sheet of dielectric material coated on each side with a thin layer of copper. The copper will then be machined away leaving only the patches and feedline. Since the antenna design requires two separate layers of material the layers must also be bonded. After the machined material is bonded together a standard RF connector will be connected to the transmission line so the antenna can interface with RF test equipment.

5.1.1 Milling

The first step of the fabrication process is machining the dielectric material. Milling is the standard machining method used to remove copper from a substrate. Other methods do exist, however they require the use of hazardous chemicals and were not used for this antenna.

A mill removes material to create geometries out of copper by moving a spinning end mill across the plane of the material. The depth of the end mill is set to only remove the copper and little to none of the substrate material. Modern mills are often computer controlled by custom software interfacing that can import standard computer aided drafting (CAD) files. For this antenna the antenna design was exported from HFSS in the form of a .dxf file. The exported .dxf file was then modified using AutoCAD, the area of the ground plane and substrate material was increased from 26.67mm square to 70mm x 78mm to allow at least a wavelength of substrate from each patch to each edge. This was done so the antenna would behave more closely to the simulated antenna with an infinite ground plane. Once the CAD files were imported into the software, the material was placed on the milling table, and the end mill depth set properly the milling was ready to start.

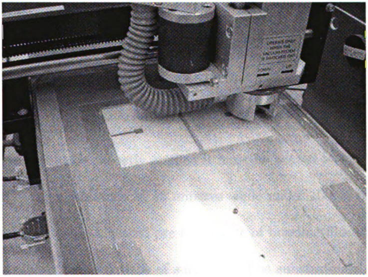

Figure 5.1. Antenna being Milled.

The process is automated requiring the user to only switch end mills and adjust end mill depth if required. The end mills need to be switched in two situations. First, as a mill is used the edges become dull and starts making rough cuts. Second, different sized end mills are used for different situations. In areas of fine detail, around patches and feedline, a smaller end mill should be used. If too large of an end mill is used for detailed areas of the antenna can be damaged(Figure 5.2). For larger open areas larger mills should be used to decrease the time spent machining the material. For this antenna design a $10mil$ diameter end mill was used around the patches and feedline and a $39mil$ diameter end mill was used for clearing out large open areas of copper.

Once the copper surrounding the patches and feedlines has been removed the remaining copper can also be peeled off using razors blades. This saves machine time and can produce better results becasue The substrates do not always have uniform thickness so large areas of copper are removed evenly by the end mill (Figure 5.3). Once the two slabs of substrate have been successfully milled they are ready to be bonded.

5.1.2 Bonding

For the bonding film to be properly applied it must be heated to 428^oF and held at that temperature for a minimum of 15 minutes while under $100psi$ of pressure [10]. This is accomplished using a heated press. A piece of bonding film the same size as the antenna is placed between slabs of substrate. The substrate slabs and bonding film are aligned vertically placed in the press. In order to monitor the temperature a

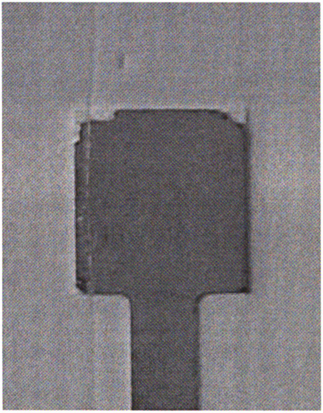

Figure 5.2. Patch damaged by wrong size end mill.

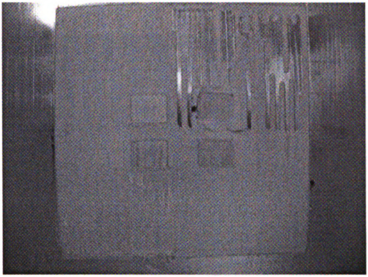

Figure 5.3. Large areas of copper missed by mill.

thermocouple temperature sensor was positioned in the press near the antenna. The press is then turned on and the heating process begins. At this time the antenna is also put under $100psi$ of pressure. After the antenna is held at 428^oF for 15 minutes the heated is turned off and the antenna cools off under pressure. Finally, the cooled off antenna can be removed from the press and is ready to have a connector attached.

5.1.3 Attaching Feed

In order for measurements to be performed on the antenna a way to interface with RF test equipment needs to be employed. For this antenna an SMA connector that is designed to have a 50Ω impedance up to $18GHz$ was used [1]. The center conductor of the SMA connector was soldered to the top of the microstrip feedline (Figure 5.4), the outer conductor was soldered to the ground plane of the antenna(Figure 5.5).

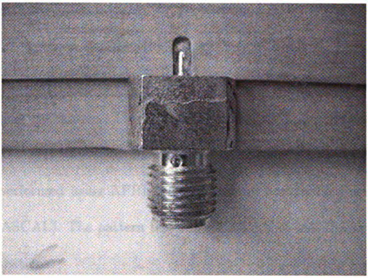

Figure 5.4. Center conductor of SMA connector soldered to microstrip feedline.

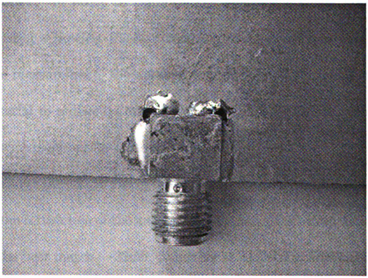

Figure 5.5. Outer conductor of SMA connector soldered to antenna ground plane.

5.2 Testing

Once the SMA connector is attached to the antenna a series of tests on the antenna need to be performed to evaluate the antenna's performance. First a single port impedance test will be performed. This test will indicate how good of a match the antenna has with the source. The impedance data can be plotted on smith charts and VSWR plots, and bandwidth information can be found. Also, a series of pattern tests will be performed using AFRL's Radiation and Scattering Compact Antenna Laboratory(RASCAL). The pattern test will indicate how well the antenna radiates in different directions.

5.2.1 Single Port Impedance

AFRL's Hewlett Packard 8510 Network Analyzer was used to measure the antenna's impedance. The analyzer was setup to measure the impedance of the antenna from $10GHz$ to $15GHz$. In order to calibrate the analyzer a single port short, open, load method using a Hewlett Packard 8505B calibration kit was employed. During the impedance measurements the antenna was positioned to radiate into a piece of absorbing material to reduce its interaction with the environment. The results from the impedance measurement are shown below.

Figure 5.6 shows the return loss of the antenna obtained from experimental testing. It shows that the return loss of the antenna is less than -10dB from about $11.3GHz$ to $14GHz$ with the best match, $-32dB$, occurring at $11.7GHz$. The simulated antenna indicated a similar range of frequencies with a low return loss, $10.8GHz$ to $13.3GHz$, with a best match of $-20dB$ occurring at $12.6GHz$. There is some difference be-

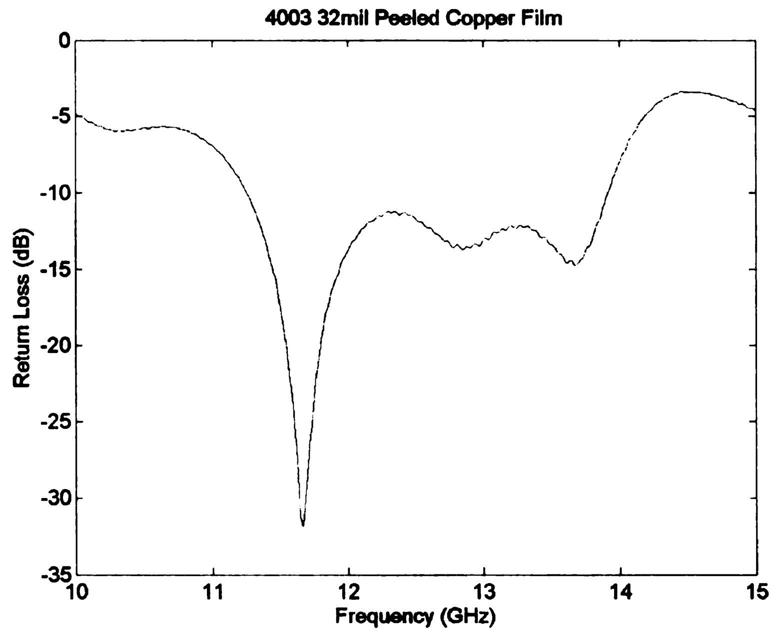

Figure 5.6. Return loss of antenna from experimental data.

tween simulated and experimental results. The simulated antenna was assumed to have an infinite ground plane, this obviously is not possible in practice. The simulated antenna also did not include the SMA connector, the antenna could be having some interactions with the connector. Fortunately, in this situation the experimental data is slightly better for the Mini-UAV application. The center of the experimental bandwidth, $12.65GHz$, is closer to the design center frequency, $12.5GHz$, than the simulation, $12.25GHz$. The experimental bandwidth is also higher, 21.5% compared to the simulations 20.6%.

Figure 5.7 shows the VSWR of the tested antenna. VSWR is another way to format the return loss data, so the same conclusions can be made from this data. The best match, where the VSWR is closest to one, occurs at $11.6GHz$ and the

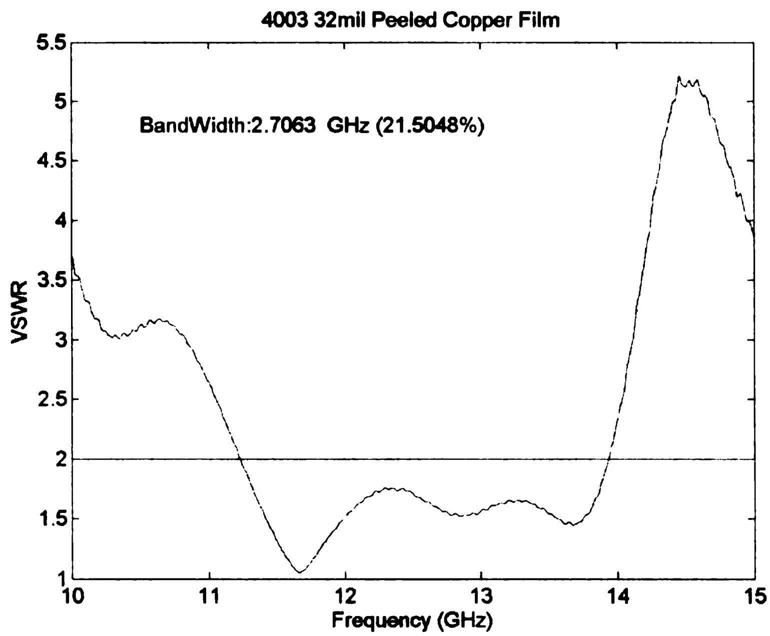

Figure 5.7. VSWR of antenna from experimental data.

antenna again is shown to have a bandwidth of 21.5%.

Figure 5.8 shows the smith chart of the measured impedance. The loops around the center indicate the broadband match that was observed above. The smithchart of the experimental data shows multiple loops around the center in contrast the simulated antennas single loop. This indicates the elements of the experimental antenna coupling together slightly differently than in simulation, however it results in the favorable characteristic of slightly increased bandwidth.

5.2.2 Radiation Patterns

The results from the impedance test show that the antenna will have the desired bandwidth, but the radiation pattern of the antenna is also very important. AFRL's

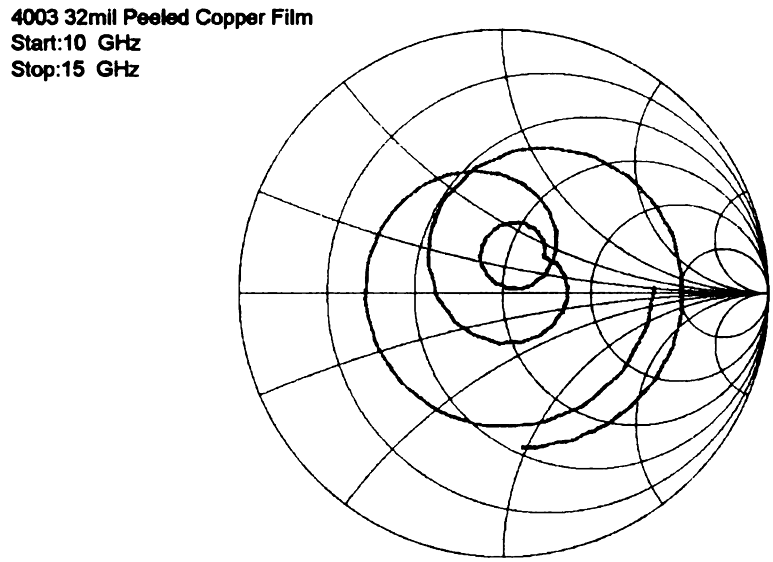

Figure 5.8. Smithchart from experimental data.

RASCAL was used to perform the radiation pattern measurements. RASCAL uses an Agilent E8362B network analyzer and an Hewlett-Packard 8349B microwave amplifier to feed a linearly polarized horn antenna. The horn antenna can be rotated to have either horizontal or vertical polarization. The waves from the horn antenna are bounced off a reflector that is designed to convert the horn's radiated waves into plane waves directed at a target antenna. As the target antenna is rotated the plane waves are used to find the far field pattern of the antenna. To test this antenna the network analyzer was setup sweep from $10GHz$ to $15GHz$ every 0.5^o from 90^o to 270^o, where 180^o corresponds to the 0^o position of the antenna in the simulations. The gain of the antenna was found by comparing its measured gain to the gain of a calibrated horn antenna measured in RASCAL .

Since this antenna is linearly polarized antenna patterns of both horizontal(E-plane) and vertical(H-Plane) polarization will be taken. The E-plane and H-plane patterns of the antenna at $12GHz$, $13GHz$, and $14GHz$ will be shown in the following figures. Figures 5.9 to 5.11 show the gain of E-plane of the antenna, the horizontal line indicates $-3dBi$ from maximum gain. Figures 5.12 to 5.14 show the polar plots of the E-plane pattern.

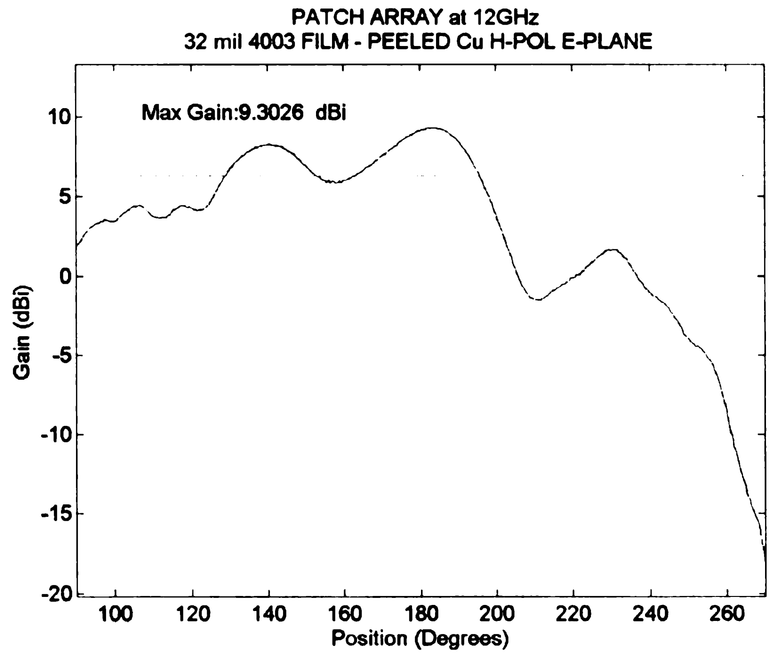

Figure 5.9. Antenna experimental E-plane gain at $12GHz$.

The experimental E-plane patterns show that there is not the simple lobe that the simulations had predicted, Figures 4.23 to 4.28. The half power beam width of the antenna in the E-plane is about 40^o. The peak gain of the patterns do all occur near

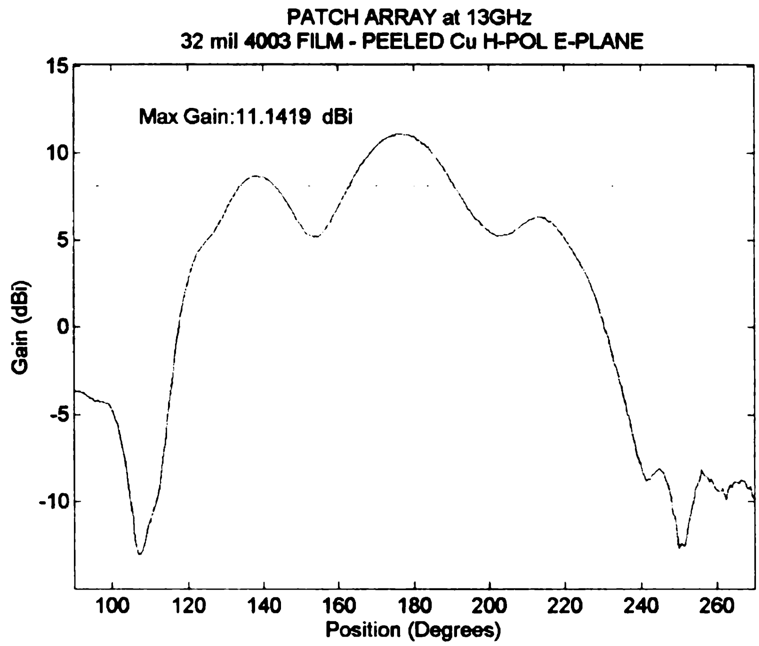

Figure 5.10. Antenna experimental E-plane gain at $13GHz$.

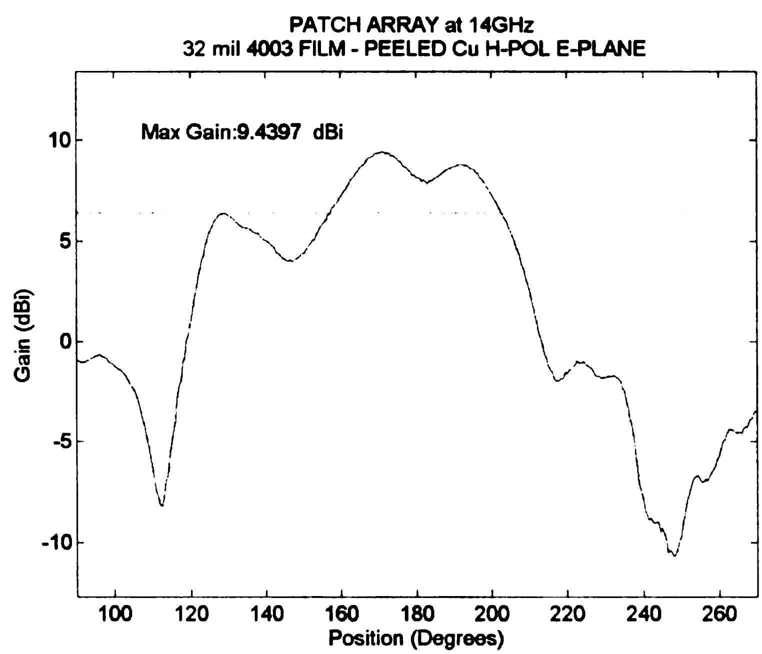

Figure 5.11. Antenna experimental E-plane gain at $14GHz$.

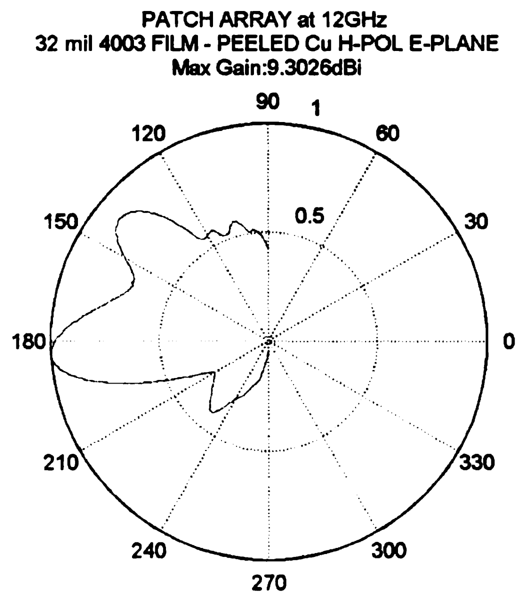

Figure 5.12. Antenna experimental E-plane pattern at $12GHz$.

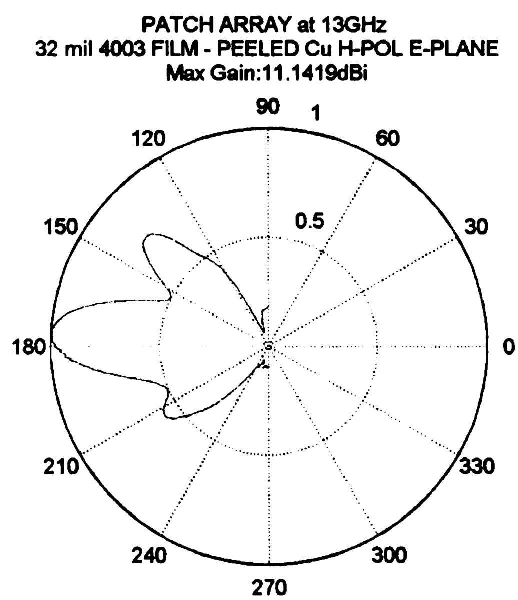

Figure 5.13. Antenna experimental E-plane pattern at $13GHz$.

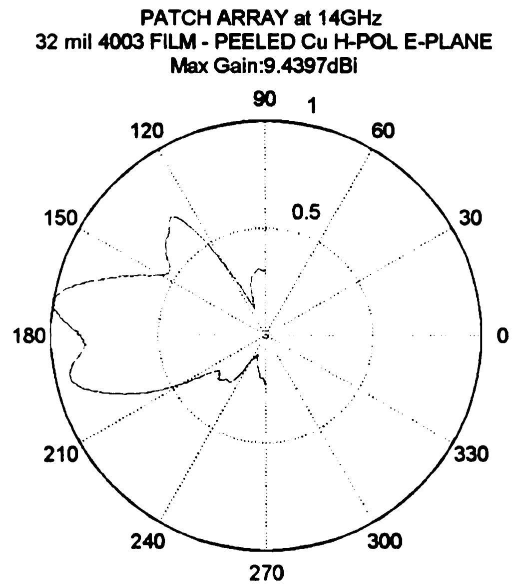

Figure 5.14. Antenna experimental E-plane pattern at $14GHz$.

broadside so the antenna is radiating in the expected direction. The inconsistency between simulation and experimentation could be partially explained by the use of a finite ground plane and an SMA connector that were not simulated. Also, in the E-plane of this antenna the feed line makes the antenna asymmetric about the axis of rotation, so the feed line could be contributing to the radiation pattern. The experimental gain of the antenna is around $2dBi$ higher than simulation in this plane. The feedline acting as a radiating element could account for this increase in gain.

Figures 5.15 to 5.17 show the gain of H-plane of the antenna, the horizontal line indicates $-3dBi$ from maximum gain. Figures 5.18 to 5.20 show the polar plots of the H-plane pattern.

The experimental H-plane patterns show that there is a single lobe at broadside

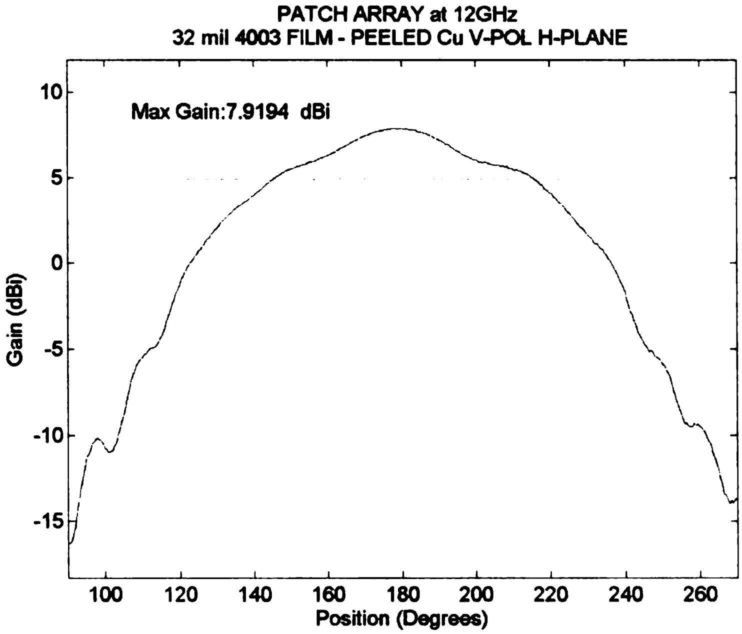

Figure 5.15. Antenna experimental H-plane gain at $12GHz$.

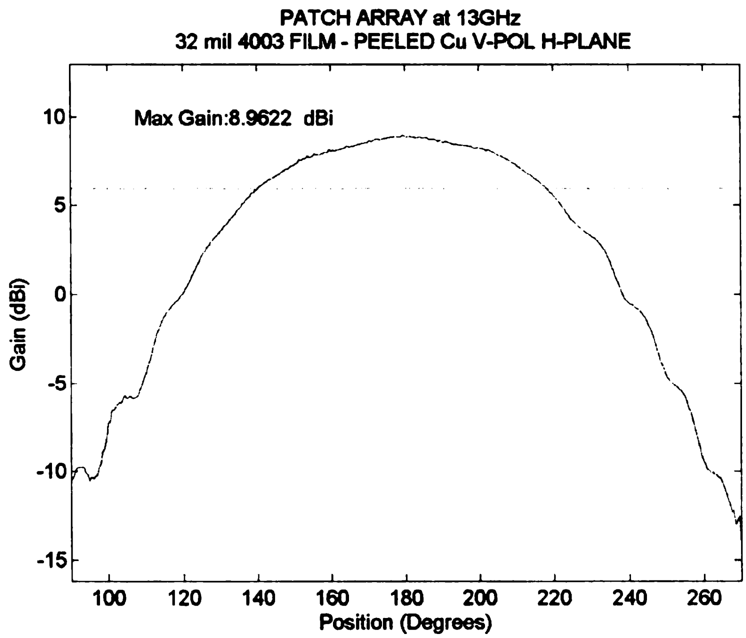

Figure 5.16. Antenna experimental H-plane gain at $13GHz$.

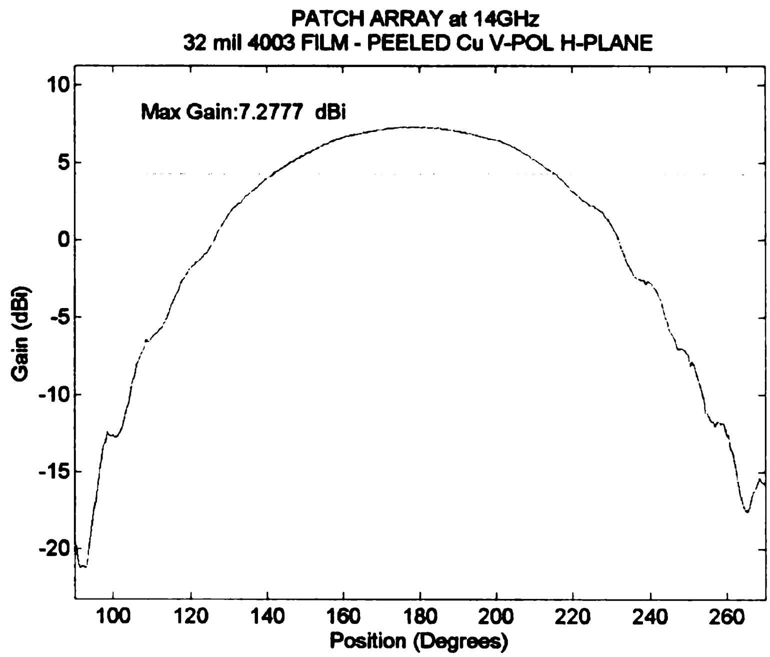

Figure 5.17. Antenna experimental H-plane gain at $14GHz$.

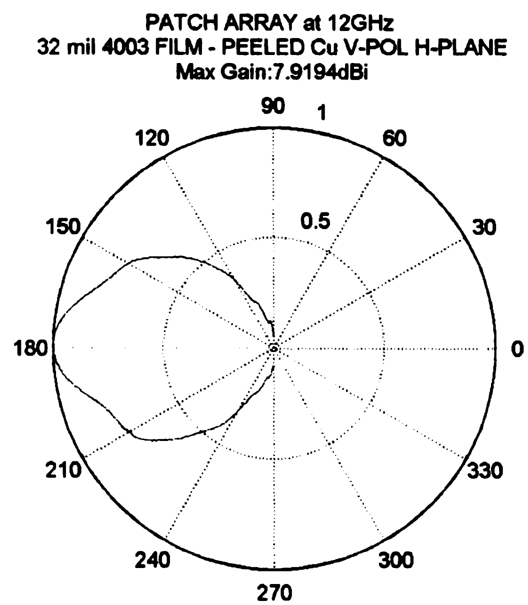

Figure 5.18. Antenna experimental H-plane pattern at $12GHz$.

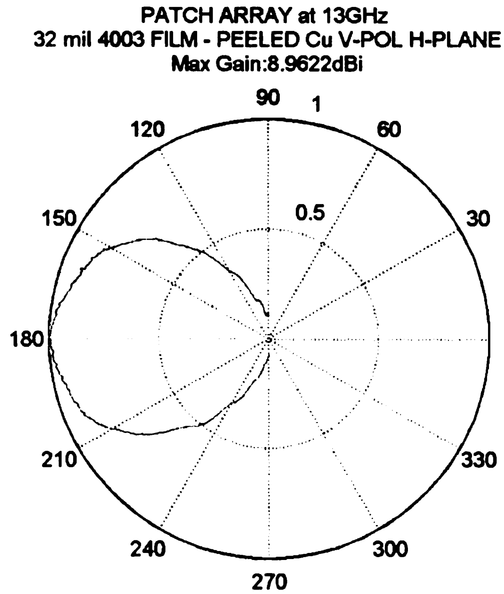

Figure 5.19. Antenna experimental H-plane pattern at $13GHz$.

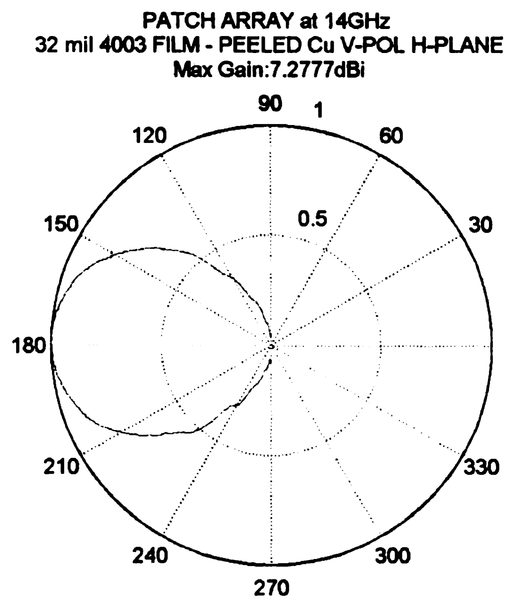

Figure 5.20. Antenna experimental H-plane pattern at $14GHz$.

that the simulations had predicted, Figures 4.29 to 4.34. The half power beam width of in the H-plane is around 80^o. In the H-plane for this antenna the feedline is along the axis of rotation, so it will always be contributing to the pattern equally. The different orientations of the feedline and the resulting patterns indicate that the feedline is probably radiating. The gain for the H-plane agrees within $0.3dBi$ for the pattern in this plane.

This chapter has described the process of taking a simulated model on a computer screen to an experimentally tested prototype. It was found that the simulated and experimental results were often similar, however never exactly the same. Most of the experimental results indicate that the antenna will operate as required for the Mini-UAV radar system. The experimental bandwidth of the antenna was found to be over 21%, higher than the required 15%, and centered at $12.65GHz$ not far from the $12.5GHz$ radar center frequency. The H-plane of the antenna has a nice single lobe pattern. However, the asymmetric E-plane pattern of the antenna does casue some concern, some approaches that will be used to attmept to resolve this issue will be presented in the following chapter.

CHAPTER 6

CONCLUSIONS AND FUTURE WORK

This thesis has produced a low profile($1.65mm$), light weight, linearly polarized patch antenna with $2.7GHz$ of bandwidth(21%) centered at $12.65GHz$ that meets the requirements of the radar sytems being designed for AFRL's Mini-UAV.

The physical requirements were meet by selecting a patch type of antenna that easily lends itself to being low profile and light weight. The patch antenna is also generally linearly polarized, but suffers from low bandwidth. In order to meet the electrical requirements, previously discovered broadbanding techniques were used in this thesis to arrive at a general high bandwidth antenna design. From the general design simulations were sued to tune the design. This tuned design was then fabricated and experimentally tested.

The simulation and experimental results are similar in most cases, often times the experimental results are slightly better. Simulations estimated a bandwidth around 20.6% centered at $12.25GHz$, while experiments show 21.5% bandwidth centered at $12.65GHz$. For the H-plane pattern, the simulated and experimental maximum gain were within $1dBi$ of each other, with a nice smooth, round lobe. The E-plane patterns are where the simulated and experimental data start to differ substantially. The experimental gain is around $2dBi$ more than the simulated. Also, the experimental E-plane pattern had a uneven lobe that did not closely resemble the simulated data. The shape of the patterns may have been affected by the test setup. Long cables capable of introducing error were used and the antenna was not positioned in a test body so interactions between the antenna and the mounting device were possible.

It is believed that deformed E-plane pattern is partially due a radiating feedline. Future work will be performed in an attempt to smooth out the E-plane pattern by reducing the radiation of the feedline. To do this a narrower feedline will be used. To keep impedance of the feedline at 50Ω a thinner lower substrate material will also be required. The thinner lower substrate will affect the dimensions of all the patches, so the antenna will need to be further tuned using the new substrates.

Once a design with a smoother E-plane field is developed it will also be of interest to transfer the design to a more flexible but more difficult to machine material, such as Rogers 3003, to allow the feedline to be bent around to connect to the RF source that will be located behind the antenna. Slight design changes will be required to account for the lower dielectric constant of the new material.

The final improvement to the antenna design will be to position the final antenna design into an array to improve gain. This will require additional tweaks to the patch dimensions since there will be more antenna elements coupling together.

BIBLIOGRAPHY

BIBLIOGRAPHY

[1] Amphenol, *Amphenol RF - SMA Connector Series*, Amphenol RF, 2005.

[2] Ansoft, *Ansoft Corporation - HFSS*, Ansoft Corporation, 2008.

[3] C. A. Balanis, *Antenna Theory Analysis and Design*, Third ed. New Jersey: John Wiley & Sons, Inc., 2005.

[4] J. A. Berrie, *Lightweight Miniature Sensor Payload for a Mini-UAV Phase I Final Report*, Dayton: BerrieHill Research Corp., 2007.

[5] R. F. Harrington, *Time-Harmonic Electromagnetic Fields*, New Jersey: John Wiley & Sons, Inc., 2001.

[6] D. R. Jackson and N.G. Alexopoulos, "Simple approximate Formulas for Input Resistance, Bandwidth, and Efficiency of a resonant Rectangular Patch", *IEEE Trans. Antennas and Propagation*, Vol. 3, 1991.

[7] J. Lagerqvist, *Design and Analysis of an Electrically Steerable Microstrip Antenna for Ground to Air Use*, in *Computer Science and Electrical Engineering.* Lulea, Sweden: Lulea University of Technology, 2002.

[8] H. Legay and L. Shafai, "New Stacked Microstrip Antenna with Large Bandwidth and High Gain", *IEE Proc.-Microw. Antennas Propagation*, Vol. 141, No. 3, 1994.

[9] D. M. Pozar, *Microwave Engineering*, Third ed. New Jersey: John Wiley & Sons, Inc., 2005.

[10] Rogers Corporation, *3001 Bonding Film Properties and Laminating Techniques*, Data Sheet 4.4.2. Arizona: Advanced Circuit Materials Divisions, 2002.

[11] Rogers Corporation, *RO3000 Series High Frequency Circuit Materials*, Data Sheet 1.3000. Arizona: Advanced Circuit Materials Divisions, 2005.

[12] Rogers Corporation, *RO4000 Series High Frequency Circuit Materials*, Data Sheet. Arizona: Advanced Circuit Materials Divisions, 2007.

[13] W. L. Stutzman and G. A. Thiele, *Antenna Theory and Design*, Second ed. New Jersey: John Wiley & Sons, Inc., 1998.

[14] J. L. Volakis, *Antenna Engineering Handbook*, Fourth ed. New York: McGraw-Hill, 2007.

[15] W. W. Math, *Useful Trig Limits*, World Web Math, 1998.